Analyzing the Effects of Hurricane Harvey on Dune Morphology and Coastline Loss Using Terrestrial Laser Scanning: A Case Study at Bryan Beach, Texas

by

Daniel Rusinek

A thesis submitted to the Department of Earth and Atmospheric Sciences

College of Natural Science and Mathematics

in partial fulfillment of the requirements for the degree of

Master of Science

in Geophysics

Chair of Committee: Guoquan Wang

Committee Member: Shuhab Khan

Committee Member: Juan Carlos Fernandez Diaz

University of Houston

May 2020

Acknowledgements

First and foremost, I would like to express my sincerest gratitude to my research advisor, Dr. Guoquan Wang, for giving me the opportunity to conduct research, for providing excellent training opportunities, and for his guidance throughout the writing of this thesis. I am also indebted to my lab colleagues, Xin Zhou, Lin Xiong, Yuhao Liu, Zachary Parra, and Brendan Cornelisonn, for their efforts in collecting field data, data processing, and equipment management and for their support throughout this process. Lastly, I would like to acknowledge Dr. Juan Carlos Fernandez Diaz and Dr. Shuhab Khan for providing data used for part of this study and for their encouragement and advice.

ABSTRACT

The East Texas Coast is the most populated coastal area in Texas, making the region especially vulnerable to rising sea levels and intensifying storms. Hurricane Harvey made landfall at Rockport, Texas, between August 17, 2017, and September 3, 2017. Several studies have used light detection and ranging (LIDAR) terrestrial laser scanning (TLS) and LIDAR airborne laser scanning (ALS) to study beach morphology and erosion. LIDAR point clouds can be gridded to create high accuracy digital elevation models (DEMs) useful for performing raster calculations in several geographic information system (GIS) software packages. This study analyzes several LIDAR TLS scans of Bryan Beach, near Freeport, Texas, taken on May 2017, September 2017, March 2018, and December 2017, to study the recovery of the beach following Harvey. This study uses volume metrics introduced by Morton (1994), in which beach recovery is defined as replenishment of the total percentage of sediment lost during a storm. Volume calculations performed on the DEMs in ArcMap showed that there was a 25% loss in sediment between May 2017 and September 2017 along the 7-km study area. By March 2018, this area had fully recovered the percentage of sediment lost and had also gained an additional 101,450,886 cubic m of sediment. However, cross-shore profile analysis showed varied local recovery responses along the coast influenced by both beach morphology and artificial constructions. Bryan Beach is nourished by a longshore drift that runs parallel to the Texas Coast. Breakwater structures such as jetties disrupt the longshore current, blocking sediment from reaching downcurrent beach areas, which results `in coastline loss. The Brazos River Delta is a salt-wedge estuary that forms when river discharge is low, as is evident from the emergence of a mouth bar after the sustained flooding and high river discharge caused by Hurricane Harvey. The jetty effect, along with the salt wedge, has resulted in significant shoreline loss along the study area.

LIST OF FIGURES

LIST OF TABLES

Chapter 1: Introduction

The East Texas Coast is one of the most heavily populated and economically active coastal regions in Texas (Figure **1**). The area hosts the Port of Houston, the city of Galveston, and several important oil refineries. Due to the area's economic value, the East Texas Coast has been significantly modified by humans for the last 100 years, and coastal developments driven by industrial expansion have drastically altered the local coastal landscape (Carlin et al., 2014). The Galveston Seawall was constructed in response to the 1900 Galveston Hurricane and was soon followed by commercial outlets, such as the Port of Houston. In 1929, the Army Corps of Engineers diverted the Brazos River 10 km south to its current location (U.S. Army Corp of Engineers, 2005), and two jetties were constructed at the old river delta to act as a new Freeport harbor.

Multiple long-term studies have investigated regions of the East Texas Coast, including Galveston and the Follet Islands, but few studies have directly observed Bryan Beach (Morton, 1994; Rodriguez et al., 1999; Guzman, 2017). One comprehensive study observed Bryan Beach from 1995 to 2004. Several other studies of this area have been conducted by students at the University of Houston; these studies analyzed T:Sacquisition techniques and the dune evolution of Bryan Beach. The ability to capture detailed spatial information has made LIDAR popular for reconstruction projects, archeology, engineering, and earth sciences. Furthermore, in recent years, LIDAR has become a popular method for studying beach morphology and quantifying storm-induced beachfront changes (Xiong et al., 2019; Zhou et al., 2015; Zhenpeng et al., 2017;

Eismann et al., 2019; Kempeneers, 2005; Glennie et al., 2013).

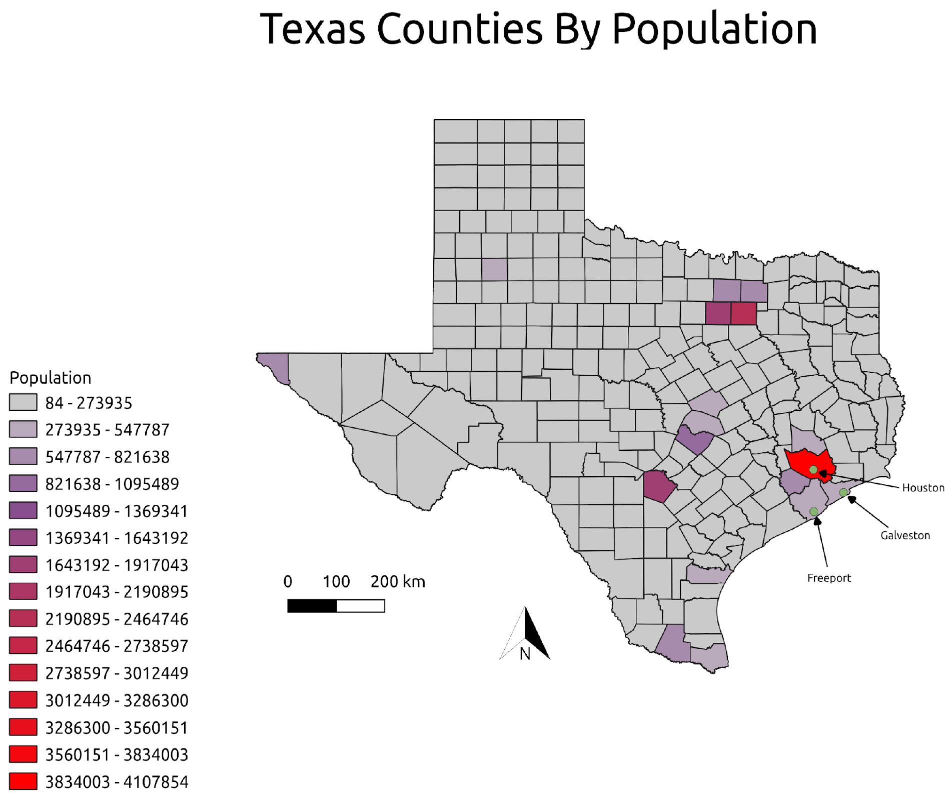

Figure 1: Texas County Map by Population. The East Texas Coast hosts several important cities and industrial areas, including Galveston, Houston, and Freeport. Harris County (red) is the largest county in Texas.

LIDAR data can also be evenly gridded into high-resolution digital elevation models (DEMs) or digital surface models (DSMs). Gridding produces a detailed raster image of a scanned area suitable for raster computations used in popular geographic information system (GIS) software, such as ArcMap, QGIS, the Geospatial Data Abstraction Library (GDAL), and the Generic Mapping Tool (GMT). Several studies have made use of LIDAR airborne laser scanning (ALS), but LIDAR TLS has gained popularity due to its ease of deployment and relative cost-effectiveness (Zhou et al., 2017). This study builds on the current knowledge base regarding Bryan Beach by monitoring the continued recovery of the region following Hurricane Harvey and determining the current state of risk posed to the coastal geomorphology.

The East Texas coastal region has two main sources of sediment, the Mississippi River and the Brazos River. The Brazos River has the largest discharge by volume of any Texas river (Carlin et al., 2014; Guzman, 2017). Sediment that is deposited in the Gulf of Mexico by the Mississippi River is mobilized by a longshore current running parallel to the Gulf Coast and travels southwest towards the Texas Coast (Morton and Mckenna, 1999). However, coastal improvements such as the Galveston Seawall and the jetties at Freeport Harbor disrupt the flow of the longshore current, causing sediment deficiencies downcurrent from the structures (Morton, 1994). Human developments and engineering projects have also disrupted the Brazos River, which further limits the amount of sediment that reaches the coast. The net-negative sediment influx results in beach erosion, because less sediment is available to replenish erosive loss (Guzman, 2017; Zhou et al., 2017). This sediment is transported downstream and deposited in the Gulf of Mexico. Once at sea, the low waves and tides in the Brazos Delta allow the sediment to be mobilized by the longshore current.

1.1: Sea-level Rise and Relative Sea-level Rise

Climate-change-induced sea-level rise is a major cause of coastline loss worldwide (Galbraith et al., 2002; Hulme et al., 2010). The entire Gulf Coast is vulnerable to the effects of climate change due to its low elevation and the increased intensity of storms, all of which are stressing the already sediment-deprived coastal environments (Carlin et al., 2014). Devoid of sediment, the coastline loses its ability to recover from dramatic weather events, which are also becoming more severe as a result of climate change.

Relative sea-level rise occurs when coastal land sinks relative to the ocean. As groundwater is withdrawn, overlying land sinks to fill in the resulting cavity, causing a relative rise in sea level. The resulting relative sea-level rise is one of the main causes of coastline loss in Texas (Jeffrey, 1993; Durnin, 2019). Growing populations in Houston and the surrounding areas (Figure **1**) and increased industrial development mean that land subsidence is a significant geologic hazard in this region (Kearns et al., 2018)

Modification of the coastal area began with the construction of the Galveston Seawall in 1902 following the Galveston Hurricane of 1900 and the opening of the Houston Seaport in 1914 (Morton and Mckenna, 1999). The effects were twofold: (1) The Galveston Seawall disrupted the longshore current, and as a result, erosion was observed immediately following the construction of the wall (Morton and Mckenna, 1999); (2) the growing Houston ship channel began demanding larger amounts of groundwater from the underlying aquifers, resulting in sea-level rise induced by land subsidence (Kearns et al., 2018).

1.2: Study Area

This study observed a 7-km stretch of beach, from the mouth of the Brazos River to the Bryan Beach Park entrance (Figure **2**), encompassing the right flank of the Brazos Delta. The beach was monitored from May 2017 to December 2018 to study the immediate and medium-term effects of Hurricane Harvey, which struck the Texas Coast between August 17, 2017 and September 2, 2017. The beach received replenishment between November 12, 2014 and March, 14, 2016, when the Texas General Land Office (GLO) deemed the beach at risk, and its replenishment is scheduled to begin between 2020 and 2022. This study identifies areas of the beach that are at high erosion risk and examines the impact of various coastal fortifications on the dune morphology of the study area.

1.3: Tropical Storms

Tropical storms and hurricanes pose a significant risk to the Texas Coast. Hurricane-induced storm surge can overtop beach dune crests and cause backbeach erosion (Eisman et

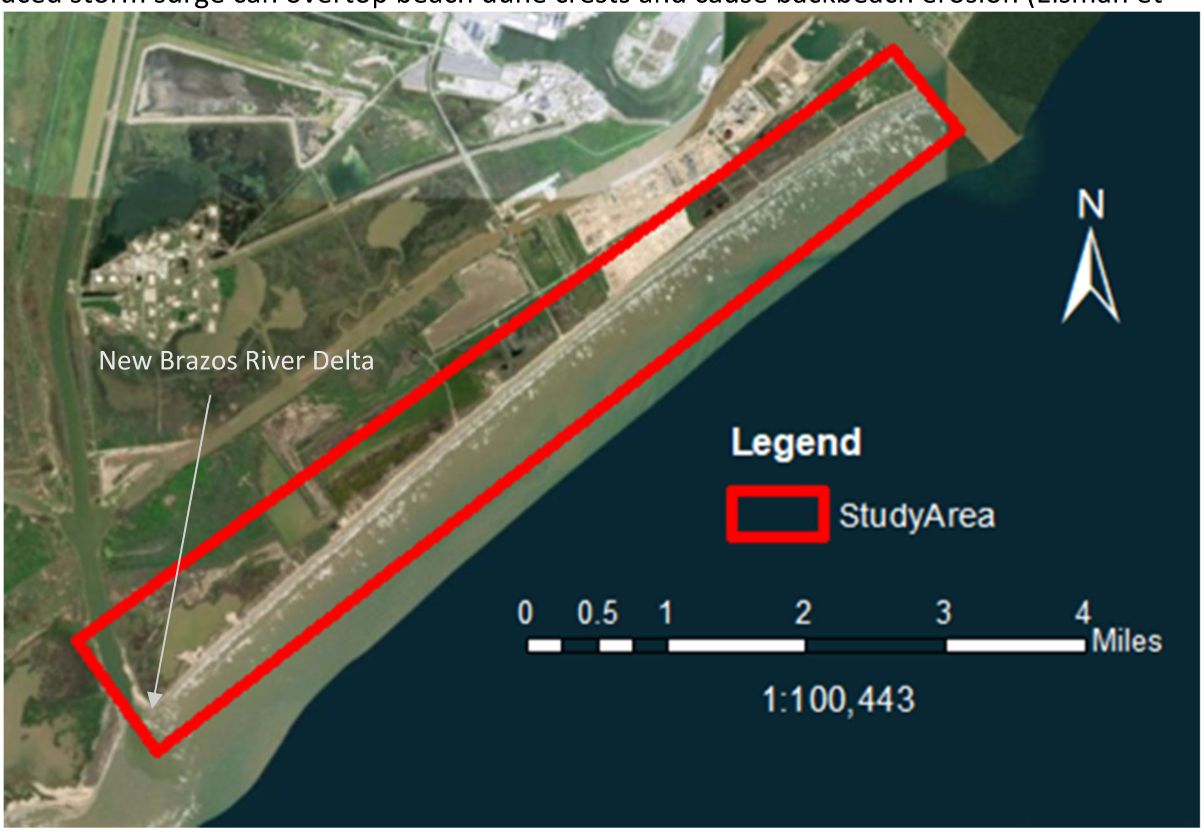

Figure 2: Study Area. The study area includes a 7-km coast stretching from the New Brazos River Delta to the Bryan Beach Park entrance.

al., 2018; Otvos, 1999). Furthermore, strong storm winds can transport large volumes of sediment through aeolian processes. Intense rain runoff may cause significant erosion from the backbeach towards the shoreline as well (Otvos, 1999). Nevertheless, it is still relatively unknown how much these short-term events affect the long-term erosion rate of the coast (Morton, 1994; Morton and Mckenna, 1999; Owen, 2017). Moreover, full recovery from a storm can vary widely, depending on many factors (Morton and Mckenna 1999; Houser et al., 2015). A study of Florida barrier islands found that dune survival during tropical storms varied according to several storm characteristics, including storm intensity, storm duration, and the frequency with which storms affect the region (Claudino-Sales et al., 2008). Also of importance are morphological parameters, including the width of the barrier island, vegetation type, the width of the dune field, the distance between the dune toe and the coastline, and dune field continuity (Figure **5**) (Claudino-Sales et al., 2008).

Hurricane Ike made landfall in the continental United States at Galveston, Texas, as a category 4 hurricane on September 13, 2008, and it remains the sixth-costliest hurricane to affect the country. The hurricane affected large parts of Louisiana and Texas, including Freeport, and caused significant damage to the dune field at Bryan Beach (Figure **26**). If not properly repaired, any dune breaches caused by storms can continue to weaken the dune structure long after the weather event has occurred. Hurricane Harvey affected the Texas Coast between August 17, 2017 and– September 2, 2017. It made landfall at Rockport, Texas, as a category 4 cyclone. The storm weakened to a category 2 storm by the time it passed by Freeport, but its slow movement allowed it to drop 33 trillion gallons of water on Texas and the surrounding Gulf Coast, causing extreme flooding in the Houston Metropolitan Area. The Brazos River discharge resulting from the rainfall also caused a red tide, visible on September 9, 2017 (Figure **3**). Along with storm surge, Hurricane Harvey caused significant geomorphological changes to Bryan Beach.

Figure 3: Pictures of Bryan Beach Taken on September 9, 2017. A red tide was visible in the delta, indicating algal growth from sediments deposited in the subaqueous delta.

1.4: Motivation and Scope

The Northeast Texas Gulf Coast is extremely vulnerable to the effects of sea-level rise and climate change, including intensifying storms. Several important oil refineries reside in Freeport, Texas, so another major storm could have an economic impact similar to that seen after Hurricane Harvey. Therefore, it is paramount to understand the health of the Freeport beaches to prepare the region for the impacts of climate change, as well as to devise plans to ensure coastal recovery.

Although many studies have focused on the initial sediment loss after storm events and initial beach deposition following the event, few studies have tracked the long-term recovery of beaches after tropical storms (Morton et al., 1994; Weymar et al., 2015; Houser and Hamilton, 2008). In a study of beach recovery conducted in 2012 on Fire Island, New York, following Hurricane Sandy, initial foredune recovery was observed within two years of the storm event (Owen, 2017). However, a long-term study of the Texas Coast after several other hurricanes found similar initial-recovery times but longer times for total recovery (Morton, 1994). Furthermore, several Freeport beaches are currently monitored by the University of Texas A&M–Corpus Christi and cataloged as part of the Coastal Habitat Restoration Geographic Information System (CHRGIS) project (Durnin, 2019; CHRGIS, 2019). However, CHRGIS contains records for only a small section of Bryan Beach (Figure **42**).

This study examines several LIDAR scans of Bryan Beach acquired between May 2017 and December 2018. These scans enable a close examination of the short- and medium-term effects of Hurricane Harvey as well as the beaches' recovery response. If the beach were to continue to be monitored, then this data could potentially be used to study the long-term (10+ years) recovery of Bryan Beach. The study area includes the right flank of the Brazos River (Figure **2**). Because this new delta is entirely human-made, it provides a unique opportunity to observe the evolution of an anthropogenic delta, that is, a delta that has evolved solely during the Anthropocene era (Carlin et al., 2014).

Chapter 2: Geologic Setting and Background Information

2.1: Coastal Setting

Bryan Beach (Figure **2**) is a predominantly wave-dominated fine-sand beach with low-lying, densely vegetated dunes (Morton et al., 1994; Carlin et al., 2014). It experiences an average wave height of 1 m and prevailing north and northeast winds, resulting in a net-longshore current that flows southwest along the coastline (Morton et al., 1994; Carlin et al.,

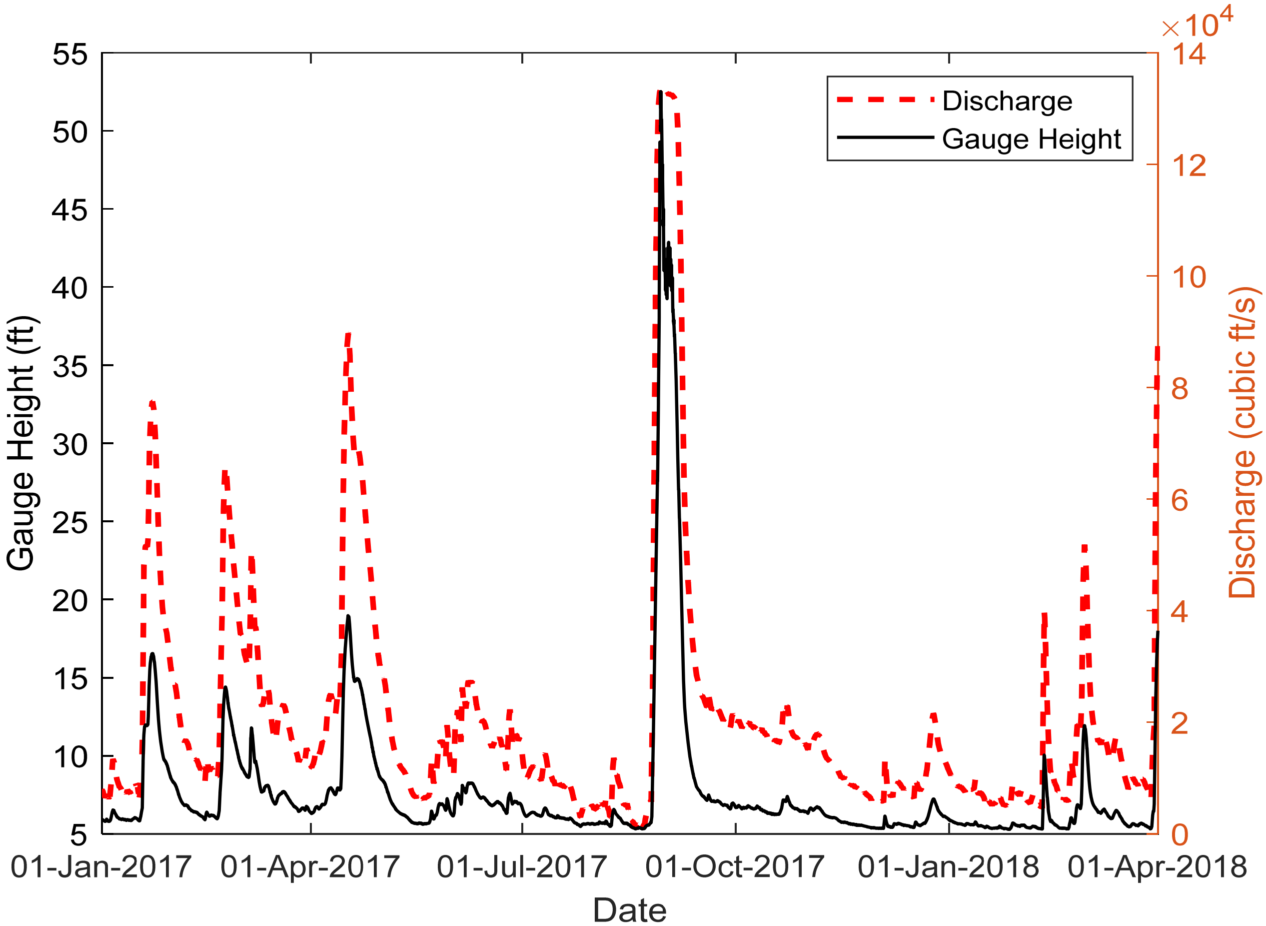

Figure 4: Brazos River Discharge and Gauge Height vs. Datetime. The plot and gauge height were measured at the Rosharon, Texas, gauge station.

2014). The longshore current is vital for the health of coastlines that lie downstream from sediment sources. Sediment from inland that has been transported to the Gulf of Mexico through various river systems is entrained by the longshore current, thus ensuring steady sediment supply to downcurrent coastlines. Yet, as previously discussed, the longshore current can be disrupted when the coastline is artificially modified to protect coastal infrastructures and developments. Some common coastal modifications include seawalls and jetties.

When taking a cross-shore profile, the beach can be broken up into several distinct zones (Morton, 1994; Puijenbroek, 2017). The beachfront consists of the foreshore and the backshore. The width of the shorefront is pivotal to the survival of beach dunes (Claudino-Sales, et al., 2008; Puijenbroek, 2017). The more area there is between the dune toe, or the base of a dune, the more protection the coastline provides against ocean waves. As waves strike against the shoreline, the waves stay within the swash zone, which is the zone defined by the limits of wave run-up and run-down. The closer the swash zone is to the dune toe, the higher the likelihood that a wave will strike the dune, and with greater force. Increased distance to the dune toe helps diffuse incident wave energy, and thus a large shorefront will lead to a healthier beach dune system (Morton, 1985; Puijenbroek, 2017).

During tropical storms, the swash zone can move drastically. Let the boundaries of the swash zone be denoted as S1 and S2. If S2 reaches close to the dune toe, the dune is likely to be subjected to scarping. Dune scarping occurs when a high-energy wave removes sediment from the base of a steep dune, causing a collapse of the sediment above, which can no longer be supported. The resulting steeper dunes often lack areas where vegetation can take hold and stabilize the dune. When S1 is below the dune crest and S2 is above it, the formation is called a swash regime (Claudino-Sales et al., 2008). Swash regimes can be very destructive for dunes, because the dunes can experience strong erosive forces from wave swash washing over the dune crest. Lastly, when S1 and S2 are above the dune crest, the dune is completely submerged; this formation is the most destructive effect of storms on beach dunes (Claudino-Sales et al., 2008). Due to the importance of the beachfront width, the beach width is to be kept above the action width, the beach nourishment trigger threshold for beginning any beach replenishment program under CEPRA (Durnin, 2019).

2.2: Factors Affecting Coastal Erosion

Several natural factors affect the usual cycle of beach erosion. Due to the angle of wave approach, the coast experiences a longshore current that runs predominantly in the northeast–southwest direction. As waves hit the shore, they hit it at an angle; due to that angle, the current tends to run in one direction. The resulting longshore current carries sediment along the shore. After the Brazos Delta was moved in 1929, sediment from the old delta was carried downshore, and two jetties were constructed to help keep the channel clear. The longshore current is also responsible for carrying sediment from the Mississippi River down the Gulf Coast to Texas.

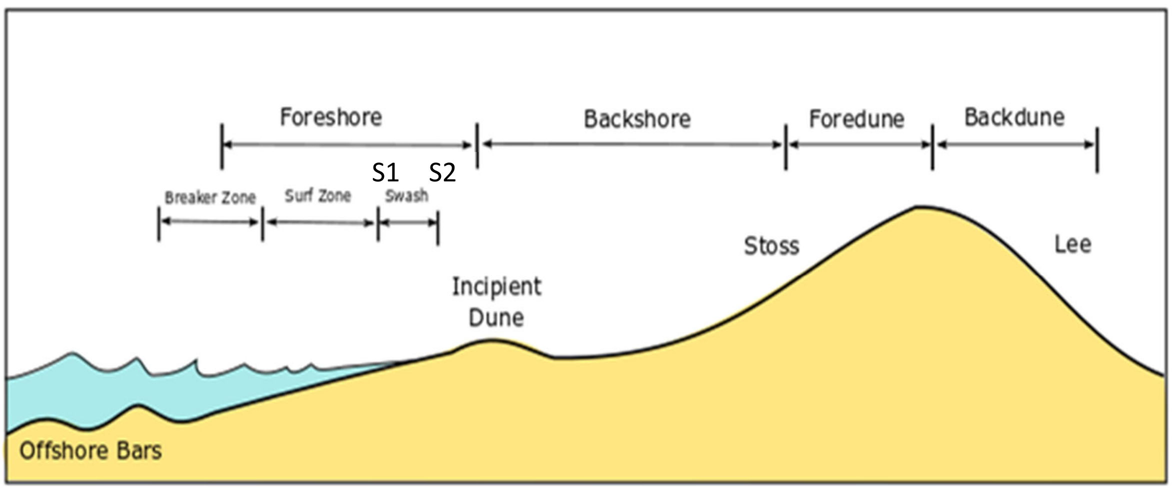

Figure 5: Beach Profile Diagram. This diagram shows a cross-shore profile of a beach with labeled parts. The beginning and end of the swash zone are labeled S1 and S2. When S1 is below the dune crest and S2 is above the dune crest, it becomes a swash regime, which has the potential to wash away sediment. When S1 and S2 are above the dune crest, this indicates that the dune is submerged and suffers extensive damage (Claudino-Sales et al., 2008; Morton and Mckenna, 1999).

Figure 6: TLS and GPS Integrated Setup. A Trimble R10 RTK GPS was mounted atop a Riegl VZ 2000 Terrestrial Laser Scanner (TLS). The GPS measures the scanner's own position (SOP) in UTM Zone 15N referenced to the NAD 83 Ellipsoid.

One of the first major human modifications to the coast occurred with the construction of the Galveston Seawall in 1902. Seawalls disrupt longshore currents by causing incident waves to reflect directly back out to sea, instead of at an angle along the direction of the current (Figure **8**). These waves carry sediment with them, which, if deposited too far out to sea, will not be re-entrained by the longshore current. Consequently, downshore erosion was observed immediately after the construction of the wall (Morton and Mckenna, 1999).

A jetty is a breakwater structure constructed perpendicularly to the coast to protect or defend a harbor or stretch of coast. The jetties at Freeport, Texas (Figure **3**), were built to protect the Freeport Harbor channel. Because the jetties jut out perpendicularly to the longshore current, sediment carried by the longshore drift is blocked, causing sediment buildup on the upcurrent side of the structure and hindering sediment from moving downcurrent (Figure **9**).

The shoreline upcurrent from the jetty advanced after the construction of the breakwater structures, but erosion started again after the mouth of the Brazos River was diverted to its current location in 1929 by the Army Corp of Engineers (Figure **4**) (Rodriguez et al., 2000; Morton and Mckenna, 1999; Morton et al., 1990). After the river mouth was diverted, the study area lost a sediment source in the Brazos River. Historical observations from Sargent, Texas, about 26 km southwest of the Brazos Delta, show an erosion rate of more than 12 ft/year, making it one of the fastest-eroding beaches in Texas (U.S. Army Corp of Engineers, 2005).

(a)

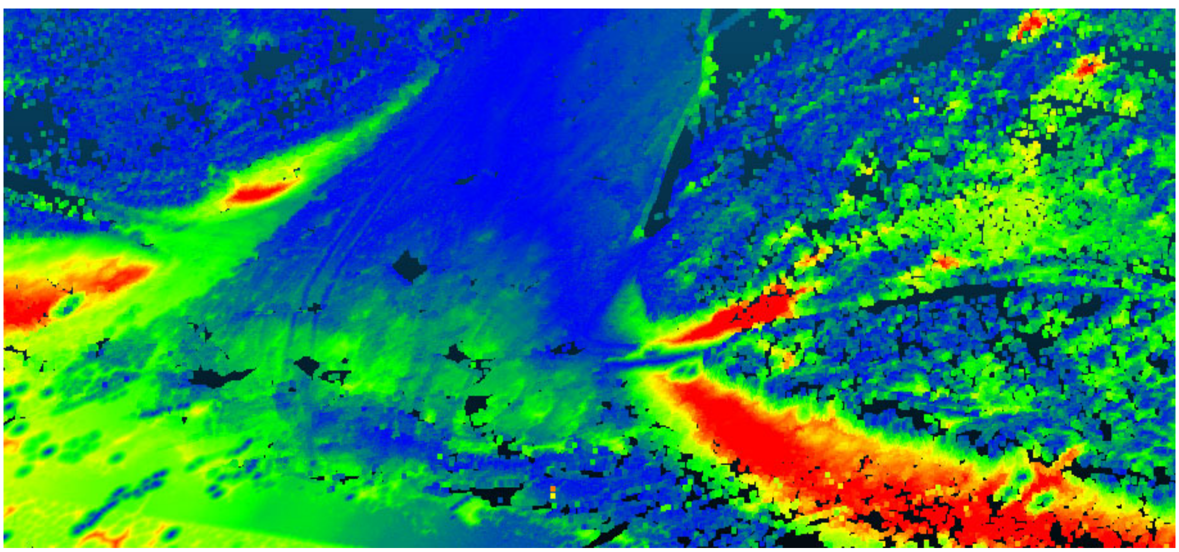

(b)

Figure 7: (a) Dune Blowout at Bryan Beach Located Approximately 0.6 km Northeast from the Brazos River Delta. (b) Cloud-to-cloud (C2C) Image of Dune Blowout. (c) Showing erosion between May 09, 2017, and September 9, 2017. The erosion at the dune base indicates that dune scarping occurred during Hurricane Harvey in this area.

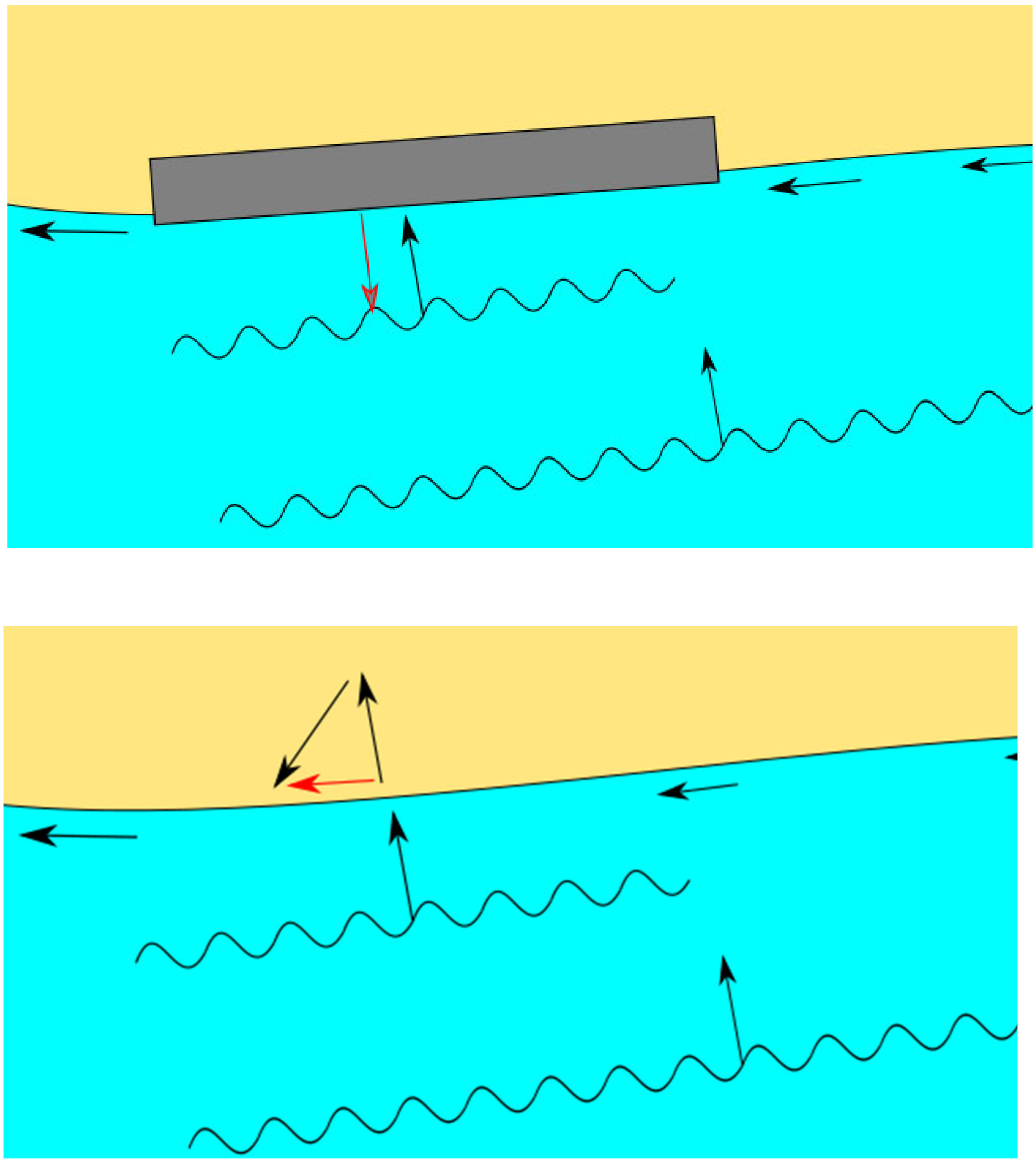

Figure 8: Seawalls' Effect on Longshore Current and Deposition.
Top: Incident waves, which hit at an angle, continue travelling when they retreat back out to sea. The cumulative effect from the angled wave run-up and run-down results in a longshore current that carries sediment to new beaches downstream.
Bottom: The construction of a seawall disrupts the longshore current by reflecting incident waves back out to sea. The reflected waves deposit their entrained sediment away from the longshore current, resulting in a net loss of sediment in the littoral cell (Morton and Mckenna, 1999).

The study area has been replenished artificially by the Texas GLO to compensate for the sediment lost through coastal erosion and from tropical storms. The last major beach replenishment project lasted from November 12, 2014, to March, 14, 2016, and included the planting of pine trees and other vegetation as well as the addition of sediment.

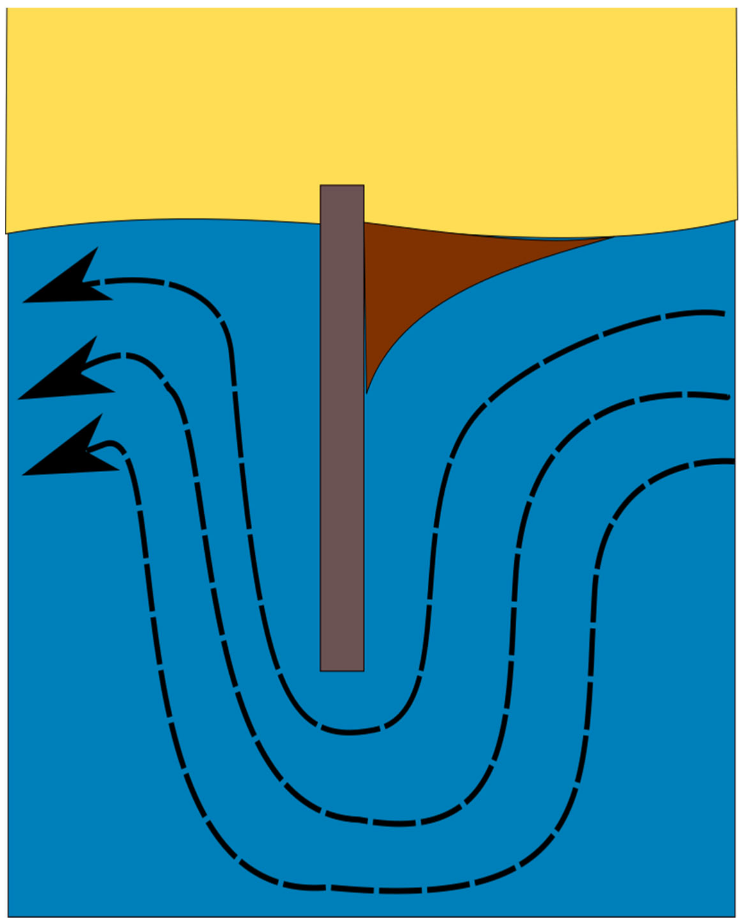

Figure 9: Jetty–Longshore Drift Interaction.
Jetties are breakwater structures that extend out into the ocean, perpendicular to the coast. Jetties block longshore drifts and cause sediment buildup on the upcurrent side.

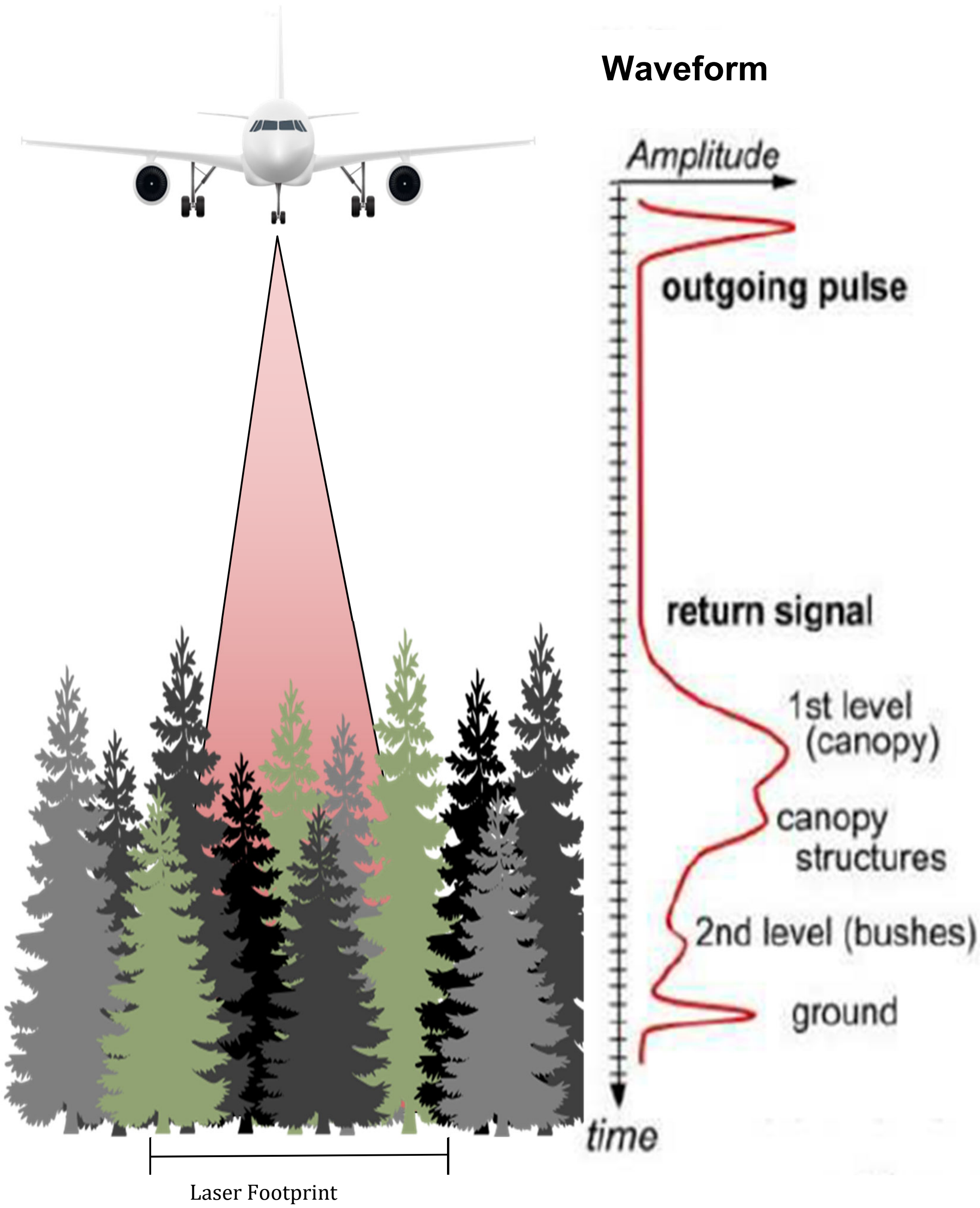

Figure 10: Airborne Laser Scanning (ALS) Diagram and Waveform. ALS fires laser pulses from an airplane that diffuse outward as they travel to the ground. As the laser pulse encounters the different forest stories, portions of the return are measured by the sensor as a pulse on the waveform (Glennie et al., 2013).

Despite artificial replenishment, the jetties still disrupt the natural longshore current, which causes accumulation of sediment on one side of the jetty and sediment depletion on the downcurrent side (Figure **9**). Consequently, Bryan Beach receives less sediment, because it resides downcurrent from the Quintana Jetty and can become sediment starved.

Chapter 3: Methods

3.1: Introduction to LIDAR and GPS

Light detection and ranging (LIDAR) is an active remote sensing method that measures the distance to a point in space by measuring the two-way travel of a laser pulse fired from the sensor. The instrument scans 3D spaces by firing off millions of laser pulses, which results in a point cloud representing the scanned area (Figure **12**). There are three commonly used methods for deploying LIDAR: ALS, TLS, and spaceborne laser scanning.

ALS requires flying over areas of study and scanning them from above with a downward-pointing LIDAR (Figure **10**). The LIDAR also contains a mirror attached to a motor that deflects the fired pulses in a sweeping motion. Combined with the forward movement of the plane, the scanner can capture a large area. The airplane must be equipped with an inertial mass unit (IMU), which accurately detects the planes' pitch, roll, and yaw, and a GPS receiver, which measures the X, Y, and Z location of the plane. These six parameters allow users to solve for the 3D location of each laser return.

When a pulse is fired, the pulse diffuses out. Once the pulse hits the ground, it can be several times larger in diameter than it was when fired. The area covered by this pulse is called the laser footprint. The outgoing pulse produces a waveform. As the pulse travels to the ground, it can be partially deflected by objects such as tree branches. When it returns to the sensor, the returning energy or echo is interpreted as a pulse (Figure **10**).

TLS operates on many of the same principles as ALS but differs in the deployment method. TLS is typically mounted on a tripod or some other terrestrial deployment apparatus (Figure **5**). The sensor rotates and scans an area 360 degrees around it and is capable of producing results accurate to the millimeter. TLS, however, suffers from some disadvantages as compared to ALS. Because ALS moves at the relatively fixed speed of the airplane, point coverage in aerial scans is relatively uniform. TLS point coverage drops off with distance from the scanner. TLS is also affected by shadow zones caused by obstructions in the paths of the laser pulses. Multiple scans were taken at different scan positions across the beach to adjust for these shortcomings (Figure **16**), to fill in any shadow zones, and to maintain a relatively dense and uniform point cloud of the beach. TLS was therefore chosen for this study due to its cost-effectiveness and ability to capture changes in dune morphology at high resolution.

Figure 11: TLS Tripod Setup at Bryan Beach Near Freeport, Texas. The Riegl VZ 2000 TLS is elevated several meters atop a tripod to ensure a clear line of sight over the beach dune crest.

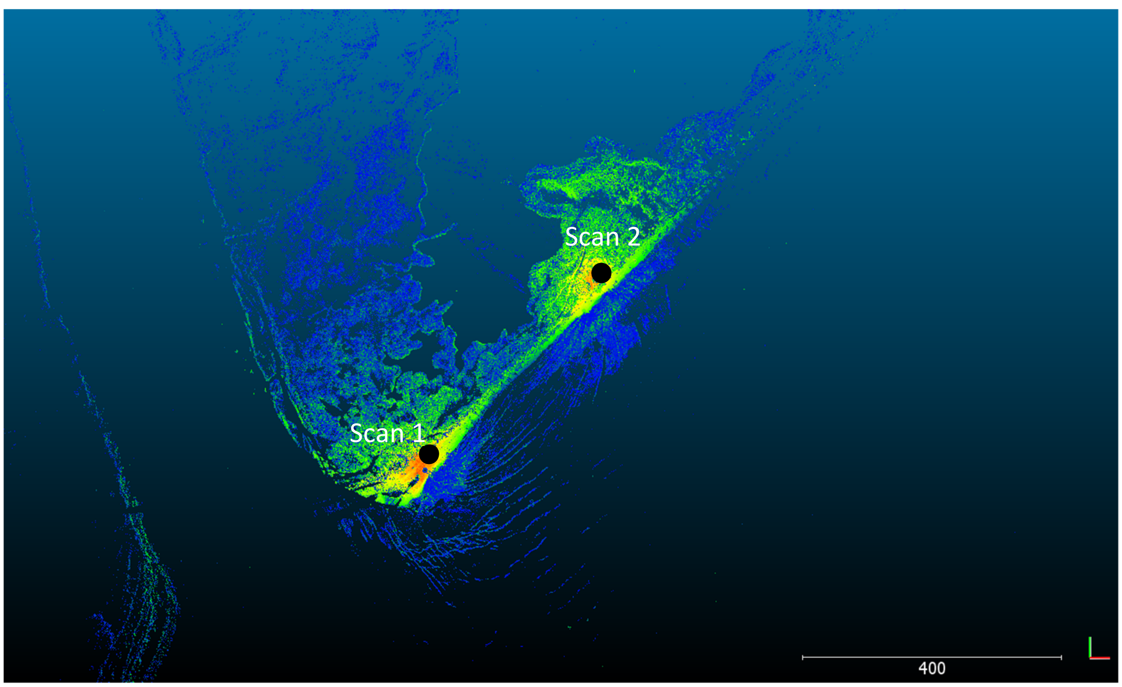

Figure 12: Combining Terrestrial Laser Scanner (TLS) Scans. Multiple scan positions are combined using the Scanners Own Position (SOP). The datum is UTM zone 15N referenced to the NAD83 Ellipsoid.

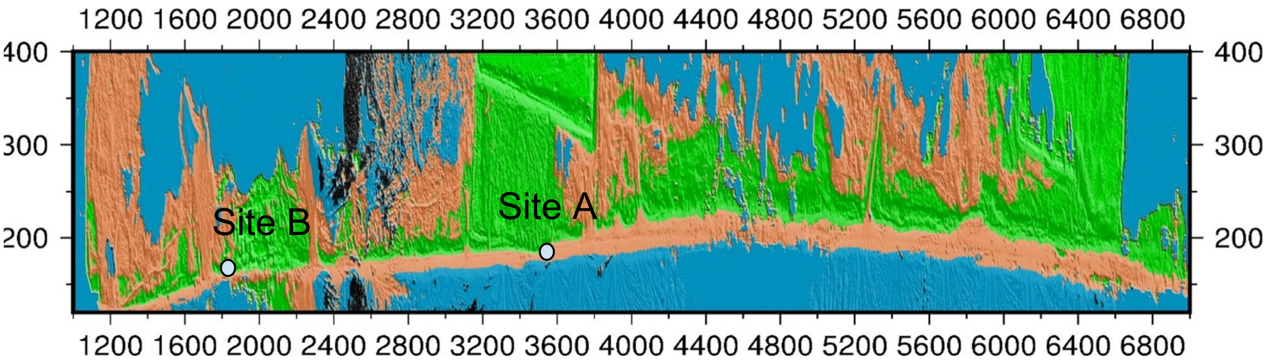

Figure 13: Digital Elevation Model of Bryan Beach Created with the Generic Mapping Tools. DEM 0.3333 x 0.3333 grid spacing was chosen. The map is projected in UTM Zone 15 and referenced to the NAD83 Surface Ellipsoid.

3.2: Sites A and B on Bryan Beach

There are two sites of particular interest along the 7-km area of study, hereafter referred to as Site A and Site B (Figure **13**). These sites were chosen for closer examination because they exhibit unique differences in beach morphology. Site A (Figure **14**) is characterized by a steep dune ridge and several pine trees that were planted during the last replenishment program, conducted from 2014 to 2016 (Durnin, 2019).

Figure 14: Pine trees Planted during the 2014–2016 Beach Replenishment. Pine trees were artificially planted during the last replenishment program. The pine trees have reinforced the dunes but are also acting similarly to a seawall. The tree roots do not allow dune retreat to compensate for sea-level rise. Photo taken December 12,

Site B (Figure **13**) is a thin section of beachfront that lies between the coast and a lagoon. The lagoon has reappeared during several periods (Claudino-Sales et al., 2008). The current backbeach lagoon was formed around 1992, during sustained flooding. As a result of the floods, the channel bar emerged, and the lagoon was created. This lagoon is mostly tidally dominated; there are two breaches in the dunes. Those breaches originally occurred during Hurricane Ike, in 2008. Figure **25** shows aerial photos of Site B before and after Hurricane Ike. The before photograph was taken on September 3, 2008, and the after photos were taken on September 13, 2008, a few days after Ike made landfall in Texas. The aerial photographs show two areas that were damaged during the storm. Unfortunately, no LIDAR data is available from 2008 for this area, but it is likely that storm surge either resulted in a swash regime or an overtop regime. Looking forward in time at the same area, the two damaged spots began to grow, indicating that they lacked any replenishment attention during the period leading up to Hurricane Harvey.

3.3: Introduction to Georeferencing and Point Gridding

Figure **12** shows the result of georeferencing two TLS scans in Freeport, Texas. Scan 1 and Scan 2 were taken independently, each with the setup shown in Figure **6**. Each of these individual scans is now in the scanner's own coordinate (SOC) system. After the scans are loaded into Riscan Pro, the GPS measurements, measured with the R10 atop the scanner, are used to assign a location for each of the scans projected in universal transverse mercator (UTM) coordinates (zone 15N) and referenced to the NAD83 Reference Ellipsoid. After completing the scan rotation, the user must indicate the reflector locations by locating them in the finished scan. Locating reflectors is normally a very simple task, because the reflector material appears in bright red in the finished scan. Once located, the scanner will fine-scan the reflector locations to ensure it has located the correct reflector. The backsighting method, therefore, requires less setup to obtain an accurate scan.

Because we now have several individual scans, the next step in processing is to combine every scan into a single point cloud. Each TLS scan is stored in the SOC system, and it must be registered into a geographic coordinate system. For this study, each scan was directly georeferenced using a backsighting algorithm. This method requires a known distance to an

Figure 15: Terrestrial Laser Scanner (TLS) Setup with Reflector. The TLS is set up atop a tripod and a reflector (circled) is placed at a distance. The TLS measures the reflector location, and the recorded coordinate is used as a tiepoint to combine each scan using the scanner's own position (SOP).

object and the azimuth between the scanner and the object to directly georeferenced scans (Lichti et al., 2005; Xiong et al., 2019). After scanning, the scanner produces a three-dimensional point in the SOC system. However, each point must be transformed into a real-world coordinate system to enable meaningful interpretations (Xiong et al., 2018). Points are transformed from the scanner's coordinate space to real-world coordinate space using the equations shown below (Lichti et al., 2005). In this study, the reflectors placed away from the scanner serve as the distant object. The high laser reflectance measured from the reflectors makes them simple to locate in each scan. Each scan is then directly

Table 1: LAS 1.2 Point Record Format. LIDAR data is stored as a .las or .laz binary file. The table indicates the byte size for each record item. Each point contains information on X,Y,Z location, intensity, return number, and other information. Point clouds can easily contain several millions of points (ASPRS, 2008).

Item	**Format**	**Size**	**Required**
X	long	4 bytes	*
Y	long	4 bytes	*
Z	long	4 bytes	*
Intensity	unsigned short	2 bytes	
Return Number	3 bits (bits 0, 1, 2)	3 bits	*
Number of Returns (given pulse)	3 bits (bits 3, 4, 5	3 bits	*
Scan Direction Flag	1 bit (bit 6)	1 bit	*
Edge of Flight Line	1 bit (bit 7)	1 bit	*
Classification	unsigned char	1 byte	*
Scan Angle Rang (-90 to +90)	unsigned char	1 byte	*
User Data	unsigned char	1 byte	
Point Source ID	unsigned short	2 bytes	*
GPS Time	double	8 bytes	*

georeferenced using the recorded GPS positions of both the scanner and the reflector, as follows:

$$\overrightarrow{r_g} = [\rho cos\alpha cos\theta \rho cos\alpha sin\theta \rho sin\alpha]^T = [XYZ]_g^T$$

The location of the scanner is given by

$$\overrightarrow{r_0} = [xyz]_s^T$$

The distant object setup station coordinates are given by

$$\overrightarrow{r_0} = [XYZ]_0^T$$

And the georeferenced object space is given by

$$\overrightarrow{r_g} = [XYZ]_g^T$$

κ is the azimuth from the setup station to the backsight station:

$$R_3(\kappa) = \begin{bmatrix} cos\kappa & sin\kappa & 0 \\ sin\kappa & cos\kappa & 0 \\ 0 & 0 & 1 \end{bmatrix}$$

Figure **14** shows the TLS setup used for this study, as well as the reflector shown circled in red. By repeating this step across the entire study area, we obtained a high-density point cloud of the beach (Figure **16**).

3.4: Point Downsampling of TLS Point Clouds

One of the biggest challenges of working with LIDAR data can be a lack of computing power. Point cloud files are often very large, and the iterative nature of point cloud computations means that even simple operations can be extremely time-consuming. The file data for this study uses the LAS 1.2 file format (Figure **16**), which is a binary format. Each point stores information about its XYZ location as well as the intensity of the laser return, the number of returns, etc. Each point, therefore, can be up to several bytes in size; with millions of points per cloud, the data files can become very large.

Several techniques can be used to reduce the computation time of algorithms. One such method requires building an octree to store all the points in the point cloud (Xiong et al., 2017). Octree filtering divides the 3D point cloud space until a base condition is met, usually the number of points per leaf node. Next, a new point replaces each octant at its center, which takes on the value of the average of the points within the octant. The octree filter significantly reduces the number of points in the point cloud while maintaining good resolution.

Due to the orientation of the coastline at Freeport, the points were rotated using the following transformation matrix (Zhou et al., 2017):

$$\begin{bmatrix} cos\theta & sin\theta & 0 & Tx \\ -sin\theta & cos\theta & 0 & Ty \\ 0 & 0 & 1 & Tz \\ 0 & 0 & 0 & 1 \end{bmatrix},$$

where θ represents the angle between true north and the shoreline after rotation and θ = 40.0π/180.0.

3.6: LIDAR Point Data Gridding

Data gridding is useful for gridding irregularly spaced points into an evenly spaced grid. A grid is laid over the data point cloud, and a new point is created at the center of each cell.

Several methods exist for interpolating the value of this center point. One of the simplest and most intuitive methods is *k*-nearest-neighbor interpolation (Figure **17**) (Zhou et al., 2014). This method finds the nearest neighbor for each center point (in red). The octree significantly reduces computation time here as well. Nearest-neighbor interpolation is a brute force approach in which each point must calculate its distance to every other point and then pick the smallest distance. This makes the algorithm an $O(N^2)$ operation, which can be costly when the number points are very large, as is the case in a point cloud. An octree allows the computer to spatially organize points in the point cloud and calculate distances for points within its octant. The algorithm is still $O(N^2)$, but it runs significantly faster because the number of points on which it must run calculations is dramatically reduced.

3.7: DEM Creation in the Generic Mapping Tool (GMT)

The DEMs for this study were created with the Generic Mapping Tools (GMT). The GMT is a collection of open-source programs suitable for geologic and geodetic processing (Wessel et al., 2013). The tools from this collection can be strung together in a BASH shell script to perform complex geoprocessing tasks, such as creating DEMs (Zhou et al., 2017). The DEMs for this

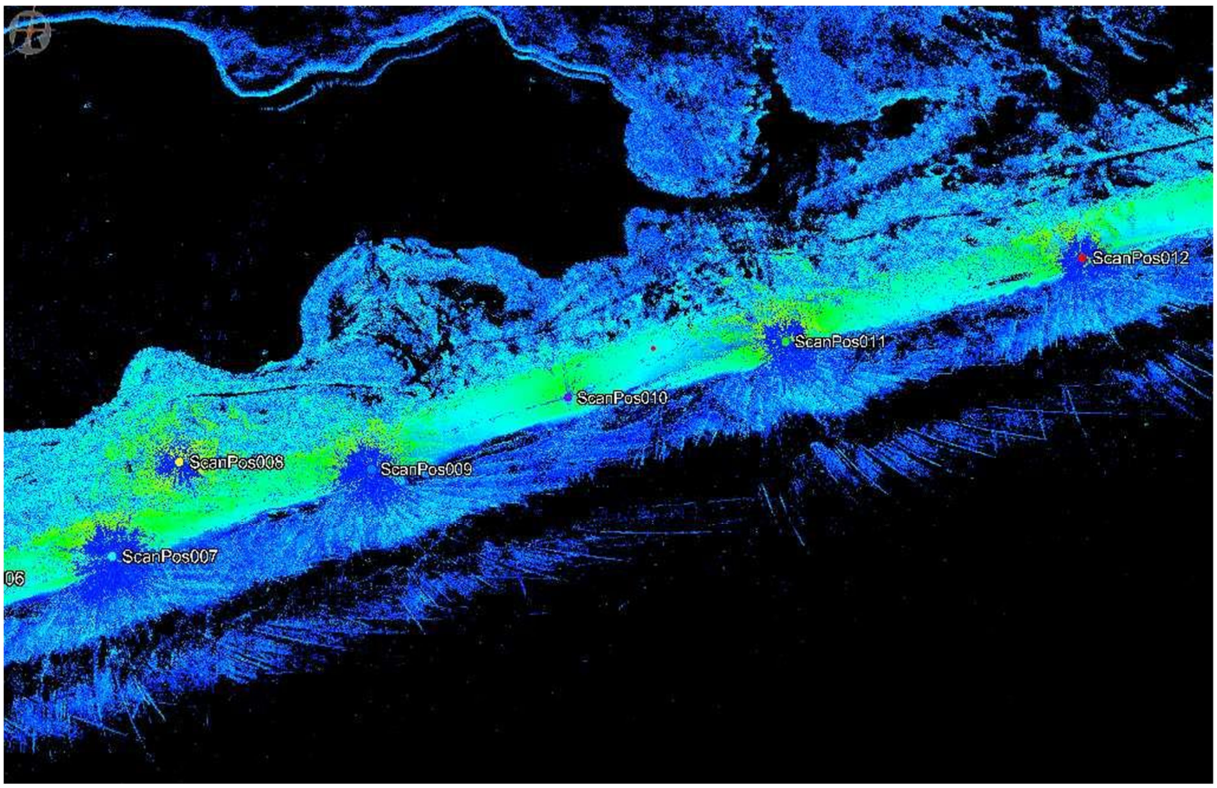

Figure 16: Combined Scans Point Density. After all scans are combined, they produce a high-density point cloud of Bryan Beach. Scans were taken about 200 m apart.

study were created with a GMT shell script provided by Zhou et al. (2017), which offers a fast and lightweight method for gridding LIDAR data into DEMs. The script invokes the near-neighbor GMT function, which calculates an average for each octree node using a cost function

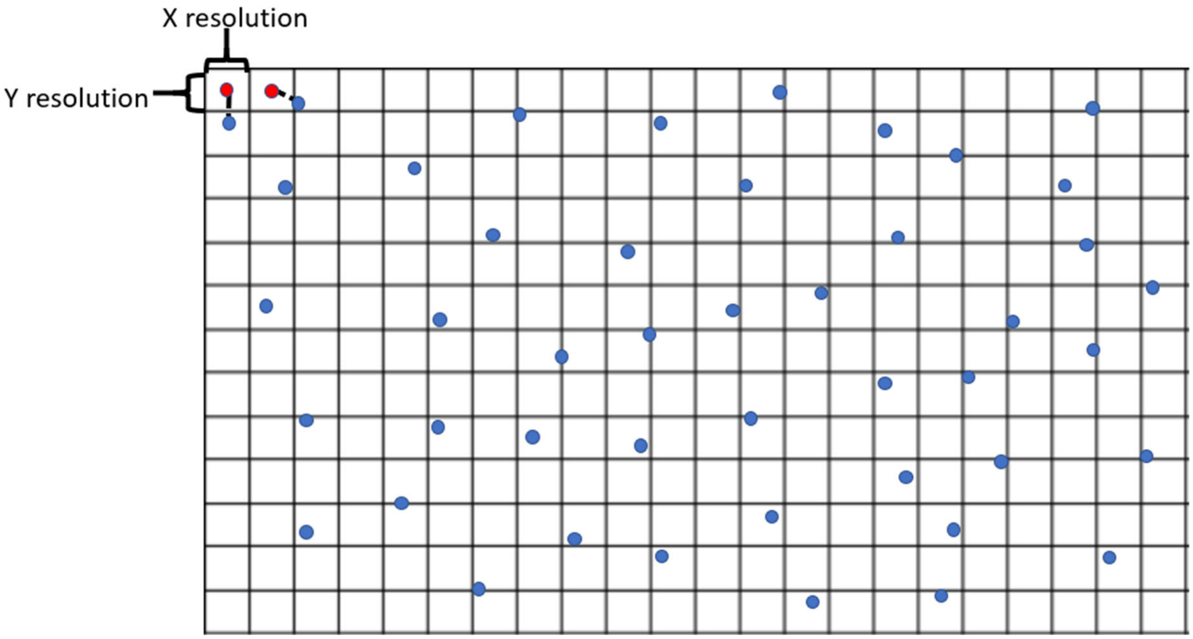

Figure 17: Basic k-Nearest-Neighbor Gridding Diagram. A grid with a chosen x and y spatial resolution is laid over the LIDAR points (blue). A new point is chosen at the center of each grid cell (red). k-nearest-neighbor is used to determine the closest LIDAR point, and the value of that point is assigned to the red point.

of distance from the node center (Wessel et al., 2013). A gridding space of 0.3333 x 0.3333 m was chosen for this study (Figure **13**).

CloudCompare is a lightweight open-source LIDAR viewing and processing software. This study makes use of the cloud-to-cloud (C2C) algorithm, which comes with the CloudCompare software. C2C is a method for comparing the relative distance between two point clouds. One cloud is used as a reference, and the algorithm computes the change in distance for each point. The algorithm is essentially a Hausdorff nearest-neighbor algorithm.

However, a local model is created around each neighbor point to estimate the true surface at that point. This gives a more precise estimate of the change between the two clouds.

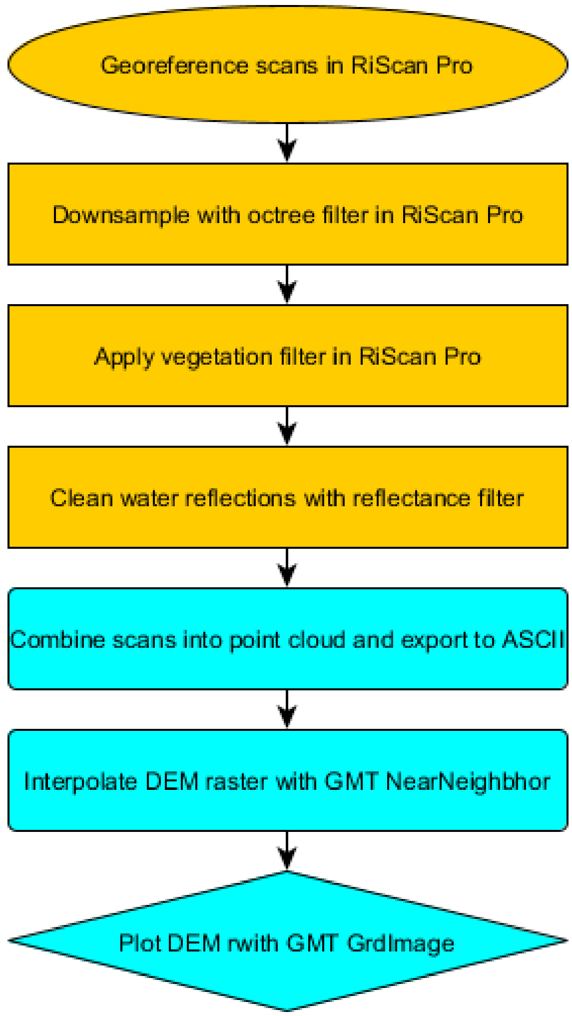

Figure 18: LIDAR to DEM Processing Workflow. The following workflow takes raw LIDAR data collected with a terrestrial laser scanner (TLS) and produces a 0.3333 x 0.3333 m digital elevation model (DEM).

Chapter 4: Measuring Beach Changes Using DEM of Bryan Beach

4.1: Accuracy Assessment

When using LIDAR data, it is important to assess the accuracy of the collected data to ensure that it corresponds to real-world coordinates. The American Society of Photogrammetry and Remote Sensing (ASPRS) recommends that acquired LIDAR data be compared using GPS measured ground control points (GCPs). The ASPRS recommends the use of at least 20 GCPs. There are many swamps that are prone to flooding, and the terrain is particularly uneven (Xiong et al., 2019). Yet, we can still obtain a good estimate of the accuracy by comparing the dataset to an ALS scan of the area obtained by the National Center for Airborne Laser Mapping (NCALM).

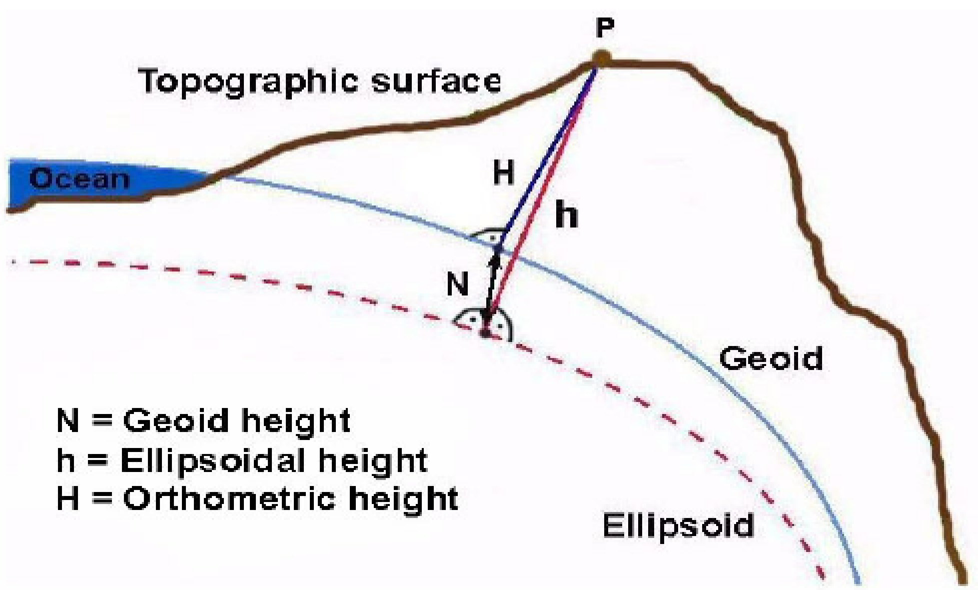

Figure 19: Relationship between geoid, orthometric (height above sea level), and ellipsoidal. The NCALM dataset was converted from ellipsoid to geoid height using the geoid height measurement from an R9 GPS at a National Geodetic Survey (NGS) marker near the study area.(Yilmaz, et. al, 2010).

The ALS dataset supplies millions of GCPs, providing that the source dataset has been processed accurately (Xiong et al., 2018). Both datasets were georeferenced in UTM zone 15N using the NAD83 ellipsoid.

Table 2: Riegl VZ 2000 Specifications

Riegl VZ 2000 LIDAR Specifications	
Effective Range	1800 m
Range Measurement Accuracy	8 mm
Pulse Rate	100 kHz
Pulse Density	Variable with distance
Line Scan Resolution	0.0015°
Frame Scan Resolution	0.005°
Field Of View	360°

Table 2 gives the specifications for the Riegl VZ 2000 TLS used in this study. The ALS scan used for this comparison was collected using a Titan Multispectral LIDAR. The scan flight was conducted at 800 m, and the scan averaged about 5 pulses per meter (Fernandez-Diaz et al., 2016). The specifications for the ALS are given in Table 3. The NCALM dataset elevations were given in ellipsoidal height (NAD83 Ellipsoid), and the TLS cloud elevations were given in orthometric height (height above sea level). An R9 GPS was placed on a geographic benchmark to calibrate the ALS points to orthometric height (Figure **20**).

Table 3: Titan Multispectral LIDAR Specifications

Titan Multisectral LIDAR Specifications	
Flight Altitude	800 m
Pulse density	$5/m^2$
Pulse Rate	125 kHz
Field Of View	60°

This bridge measurement is used to obtain the geoid height of the area. This GPS location was processed using the Online Position User System, and the geoid height of the area was calculated using the resulting GPS solution, which provides both the orthometric height and ellipsoidal height of the position (Wang and Soler, 2012). The ALS scan coverage stops just short of the geographic benchmark, but because the study area is fairly small (< 30 sq. km), the geoid height should not vary significantly. Subsequently, the NCALM dataset was shifted to convert ellipsoidal height to orthometric height, as shown in Figure **19**.

NCALM provided a DEM of the study area created from the aforementioned collected NCALM data. The DEM was created in Golden Surfer, a geospatial processing suite. The point cloud was interpolated using a kriging algorithm to a 5 x 5 m cell grid. Kriging is a geostatistical method that is widely used for the creation of DEMs. The computed shift was then applied to the computed DEM, which was compared with a DEM derived from the TLS data. Two transects were taken as shown in Figure **21** in order to compare the two DEMs.

Figure 20: National Geodetic Survey Marker at Bryan Beach, Texas. Location was measured over several hours with a Trimble R9 GPS.

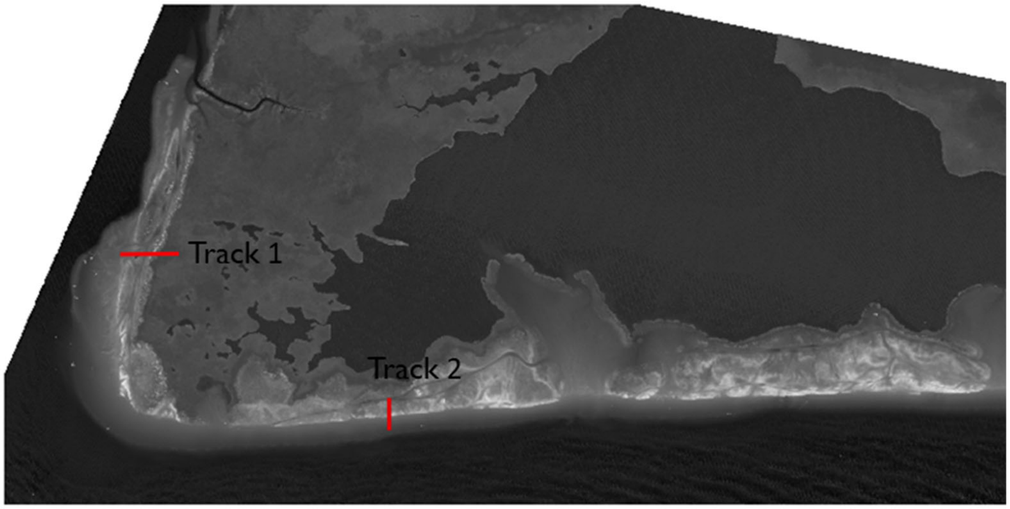

Figure 21: Tracks Chosen for NCALM-TLS Comparison.

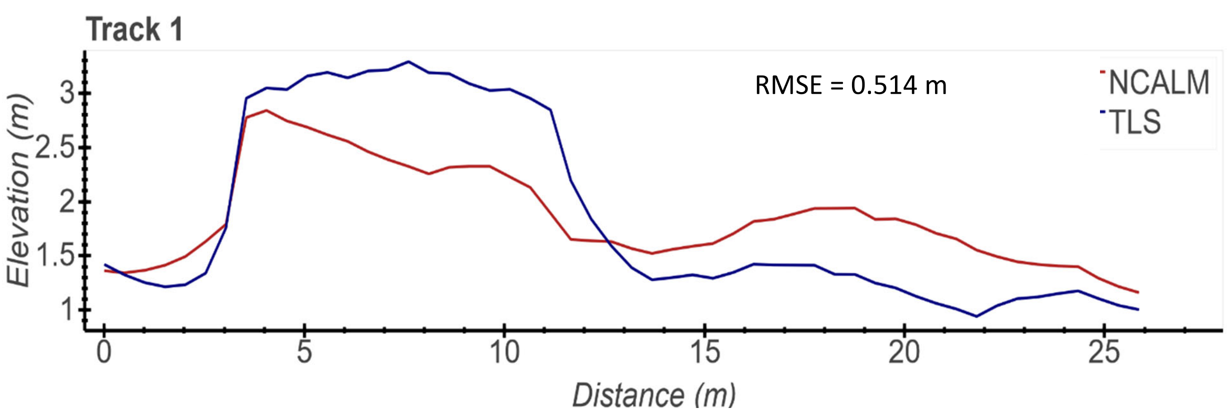

Figure 22: Comparison Track 1.

Each plot also gives a root mean square error (RMSE) calculated between the TLS and NCALM tracks for each plot. Because the Riegl and Titan scans were taken at separate times, some variation between the scans is expected as a result of natural erosive processes and shifting of dunes. Some areas of beach had been bulldozed for park cleanup, so the tracks were selected from areas that were likely unaffected by any human modifications. The track results give a reasonable estimate as the accuracy between the two datasets. The highest RMSE value calculated was 0.5, which is reasonable given the several months between both scans, and the dune extents, the start of the dune at the dune toe and the end of the dune, match considerably well.

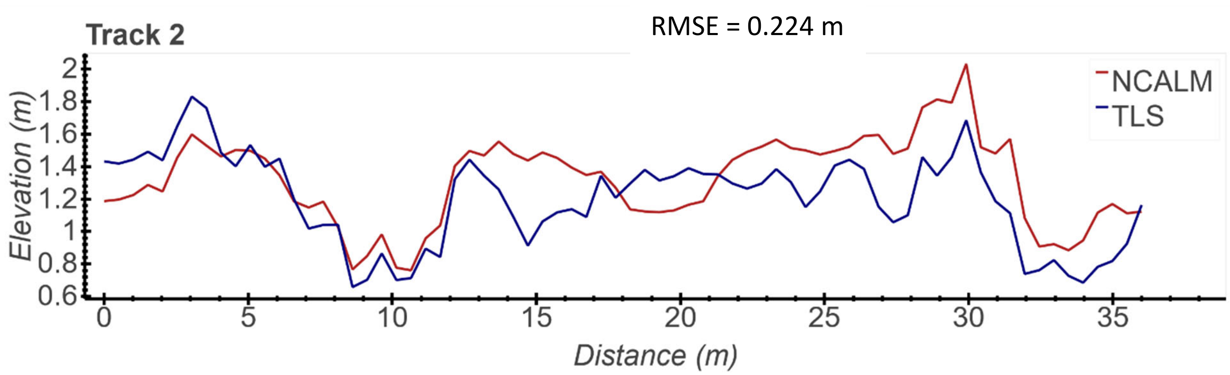

Figure 23: Comparison Track 2.

4.2: Generic Mapping Tool (GMT) Algorithms

The DEMs for this study were created with the GMT. The GMT is a collection of programs suitable for geologic and geodetic processing (Wessel et al., 2013). The DEMs for this study used a GMT shell script provided by Zhou et al. (2017). The script invokes the near-neighbor GMT function, which calculates an average for each octree node using a cost function of distance from the node center (Wessel et al., 2013). A gridding space of 0.3333 x 0.3333 m was chosen for this study (Figure **13**). The final DEM was analyzed with GMT and QGIS using several techniques. DEMs from different months were subtracted in GMT using the grdmath tool to give erosional difference maps showing areas of accretion and erosion (Figure **37**). In addition, profiles were extracted using the GMT grdtrack tool (Zhou et al., 2017). The erosional change maps were used to determine the best place for each profile. Nine profiles in total were chosen to best represent different sections of the beach and show the varied responses to Hurricane Harvey.

4.3: Transect Extraction

Transects perpendicular to the shoreline were extracted at various locations along the beach DEM (Figure **26**). Because the study area is several km in length, a number of transects were chosen to best represent all sections of the beach. It is evident that the dunes on the right half of the study area vary significantly from the dunes on the left half of the beach.

4.4: The Effects of Beachfront-width Changes on Sites A and B

As discussed above, the continuity of beach dunes has a significant effect on their long-term survival. Large breaches in the dunes can have a deteriorating effect on dunes by exposing more surface areas to erosive forces. Figure **7** shows a C2C distance measurement taken of Site A between May 2017 and September 2017. The figure clearly shows that the dune base and dune gap experienced the most erosion from Hurricane Harvey.

As explained above, the distance of the dunes from the swash zone is of great importance to overall dune health. A wide beachfront helps protect beach dunes from the

Figure 24: Site A during High Tide. During high tide, the swash zone reaches the dune toe of the reinforced dune, indicated by the red arrow. The loss of sand exposes the underlying clay. Vehicles often become trapped in the mud, and removing the vehicle further damages the beach front. Picture taken December 14, 2019.

effects of ocean waves. Because wave energy dissipates as the wave propagates towards the shore, the further a dune is from the ocean, the weaker the ocean waves will be when they hit the beach dunes. The beachfront width changes abruptly at Bryan Beach, and this has many implications for dune survival on the left half of the beach. As shown in Figure **13**, the beach dunes past point A exhibit a very different topography than the dunes on the right half of the beach. The left-beach dunes are much steeper and appear to be made of smaller grain sediments and clays. Due to the material composition and steep topography of these dunes, they are especially vulnerable not only to the effects of beach swash, but also to the effects of wind. Wind can also entrain sediment and cause it to move through saltation of sediment grains.

During high tide, water covers almost the entirety of the beachfront past point A. Beach swash now directly hits up against the vertical dunes, causing a collision regime (Morton and Mckenna, 1999). A collision regime can be detrimental to a dune system and may cause dune scarping. Moreover, when the high tide covers the beachfront, it erodes sand and exposes the underlying clay, causing vehicles to become stuck, which in turn results in further damage to the beachfront from the vehicles (Figure **23**). Figure **25a** shows a photo of Site A taken on May 16, 2014. The dune line here is relatively continuous, as opposed to the dune line captured by March 3, 2018 photos (Figure **24b**, **24c**). Looking at the beach further in the past, when Hurricane Ike affected the Texas Coast in 2008, we can see that a large section of the dune was pushed back. We observe that the ridgeline, however, appeared to move very little, if at all, suggesting that this region is more resilient against wave forces (Figure **25**).

Figure 26: Site A, Aerial View, March 23, 2018. Site A is characterized by artificially planted pine trees that were planted during a beach replenishment program between November 12, 2014, and March 14, 2016 (Texas General Land Office, 2015). The trees act similarly to a sea wall, preventing landward migration of the dune in response to coastline loss, which results in narrowing of the beachfront. Imagery from Google Earth Pro.

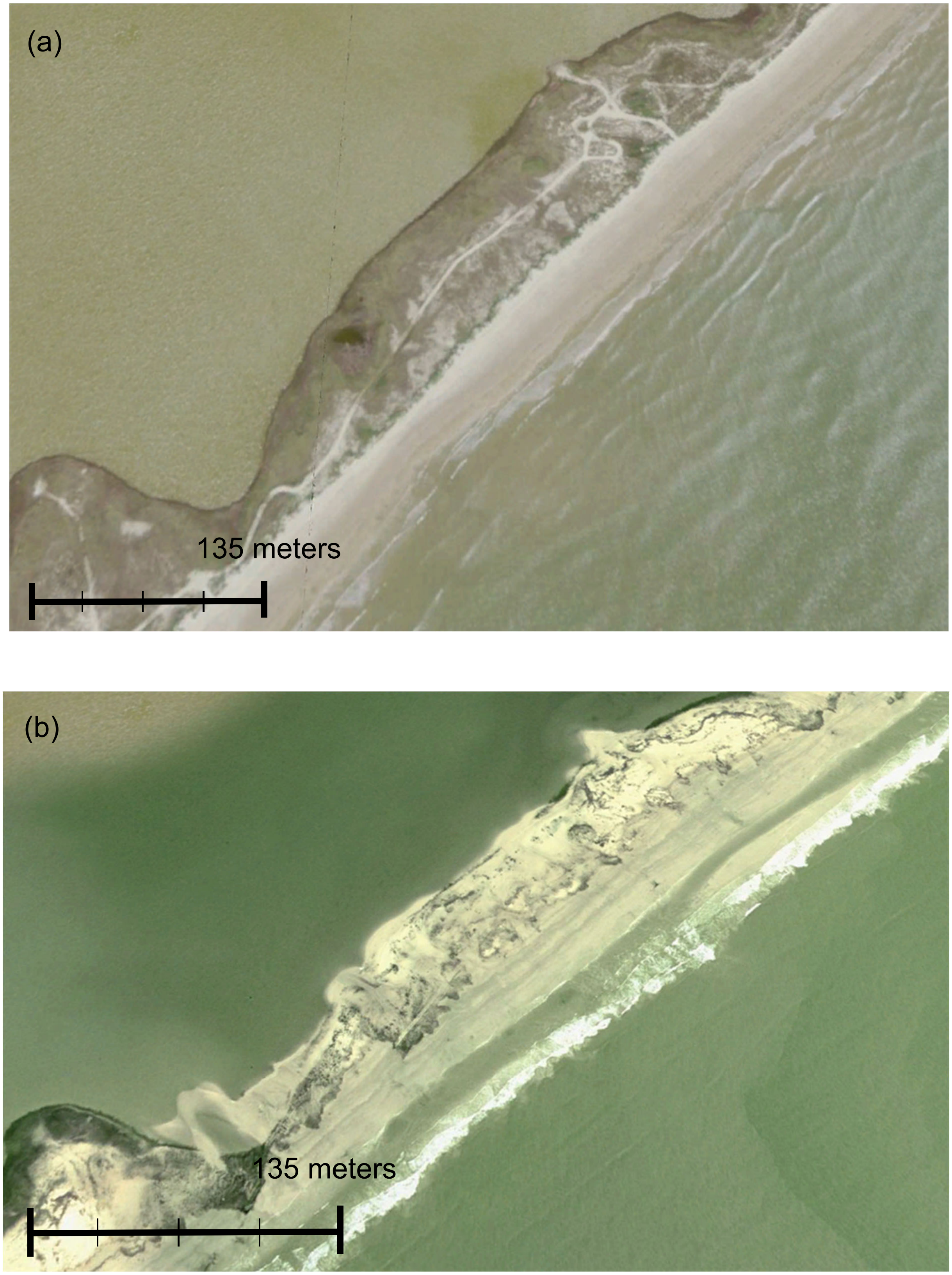
(a)
135 meters
(b)
135 meters

Figure 28: Site B, Aerial Photographs, Chronological Series. (a) Site B on September 4, 2008. (b) Site B on September 14, 2008. (c) Site B on March 22, 2018. Hurricane Ike made landfall at Galveston, Texas, near Freeport on September 13, 2008, and caused dune damage that was exacerbated by coastline loss and dune erosion. Breached dunes are more vulnerable to the effects of tidal forces and wind erosion.

Ike was a powerful category 4 hurricane, and this area appears to have recovered little by February 16, 2010. As discussed in Morton and McKenna (2014), long-term beach recovery can take up to 10 years, so it is likely that the damage observed is partly left over from Hurricane Ike's impact and that the area was still in the process of recovering in February 2014. Our team's TLS LIDAR records began in 2014; hence, we must rely on photos to assess any damage that was caused by Hurricane Ike. Moving forward to 2016, the dune line at Site A appears to have separated further, because the dune blowout continues to increase in size.

Nevertheless, it is evident that by 2019, the left dunes had retreated again. This retreat and advance of the shoreline appear to be a seasonal change that occurs on the beach as a result of stronger winter waves. During the summer, gentler waves produce a softly sloping dune topography (Guzman, 2017). The gentle slopes allow dunes to recover during the summer months, whereas in winter months, stronger waves produce steeper topography.

However, the presence of the road running behind the dunes, which also breaches the dune in several spots, could be exerting a deleterious effect on the dune by reducing the backdune region, which is vital for dune health. As seen in Figure **13**, the left dunes have been fortified with artificial planting of pine trees (Durnin, 2019), which appear to be improving the dunes' stability, but the pine trees are not present on the right dunes. Therefore, the presence of these pine trees could be a deciding factor in the dune withdrawal and advance. However, because the beach seems to be retreating despite the apparent lack of dune withdrawal, the overall beach width is still reduced and leaves the dunes vulnerable to high tide. Secondly, this area appears to have had a significant amount of its sand washed away. This evidence strongly suggests that the jetty is keeping larger-grained sand sediment from reaching Bryan Beach and replenishing it, similarly to an artificial seawall. The pine trees seem to be acting to keep this dune almost entirely in place. Because the dune cannot retreat to accommodate for landward shoreline migration caused by subsidence and sea-level rise, the result is an overall decrease of the shorefront.

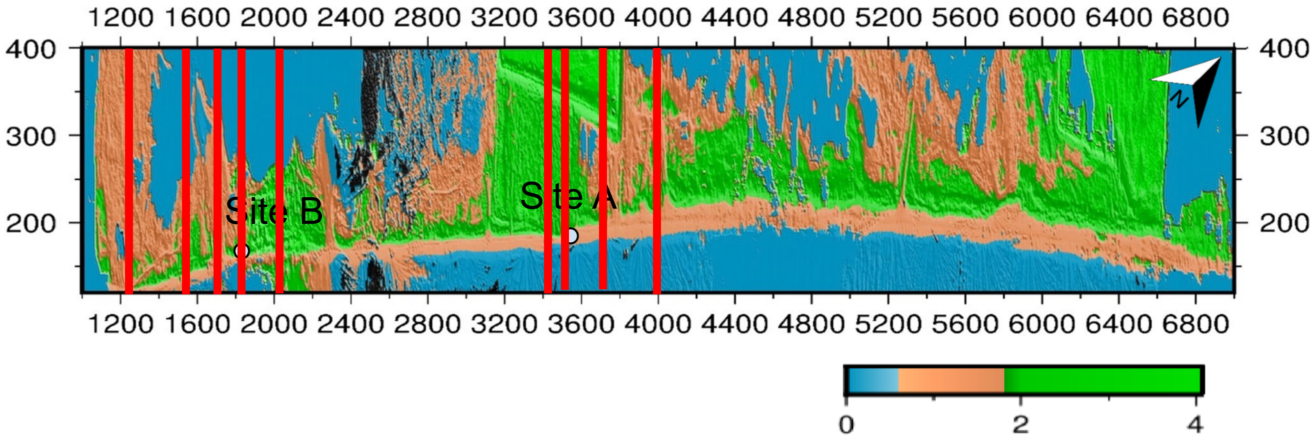

Figure 30: Track Locations. Several tracks were extracted from the final beach DEMs. Track locations are shown in red.

4.5: Shore Transect Extraction from DEM

Using the derived DEM, five cross-shore beach profiles were extracted using the GMT grdtrack tool. Profiles were chosen at several locations along the 7-km study area to accurately gauge the varied storm response along different parts of the beach (Figure **26**). Each profile was examined and compared between the separate DEMs to make observations about their recovery. It is possible that accretion of the beach face could have been affected to some extent by the bulldozing and debris clearage that took place before reopening of the beach, but these effects are difficult to quantify. Below is an analysis of each derived beach track. X1300 (Figure **27**) shows that Hurricane Harvey had a significant immediate impact on the delta region (Figure **13**). The foredune retreated and shrunk about 0.5 m. Between September 2017 and March 2018, the foredune continued to shrink, but the shoreline appeared to have stabilized, with the dune immediately behind the original foredune acting as a new foredune. By March

2018, the delta had stabilized. The track shows that Hurricane Harvey had some immediate observable effects on the dune morphology of the delta but that the beach quickly stabilized.

However, the dunes retreated almost 30 m by December 2018. Some dune shrinking and morphological changes are to be expected, because winter brings stronger wave action in this region (Guzman, 2017). However, damage caused by Hurricane Harvey likely increased the effect of the stronger winter waves on the dune morphology.

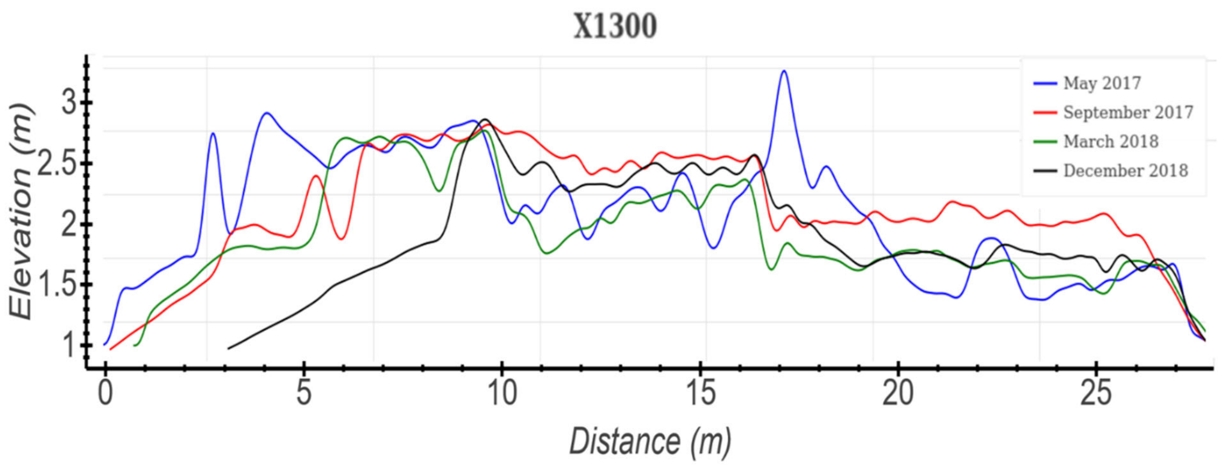

017
ember

Figure 28: Cross-shore Profile X1500. Dune retreat also occurred between May 2017 and September 2017. The dune crest remained in March 2018, and the dune crest experienced significantly less retreat than X1300.

Damaged dunes are much more likely to suffer continued damage, and a combination of aeolian and tidal forces likely contributed to the drastic change in dune position and size. It is also possible that the fall and winter of 2018 saw a stronger increase in wave activity than the winter of 2017, as is evident from the apparent stability of the dune between September 2017 and May 2018. The stability of the dune between May and September could also be attributed to excess sediment that was deposited in the river delta due to the increased river discharge from Hurricane Harvey (Figure **4**). The December 2018 dune profile does, however, show a much smoother incline from the shoreline to the dune crest, which corresponds to the deposition of a sandbar in the delta after Hurricane Harvey.

X1500 (Figure **28**) experienced a recovery similar to that of X1300. The beach profile also experienced significant damage during Hurricane Harvey. The September profile shows a much steeper profile than that of May 2017, which indicates that significant dune scarping likely occurred. However, there did not appear to be any dune blowout, that is, complete breaching of the dune. Steep slopes destabilize dunes by facilitating sediment entrainment at the dune base and can lead to further damage. This effect from the slope is evident from the

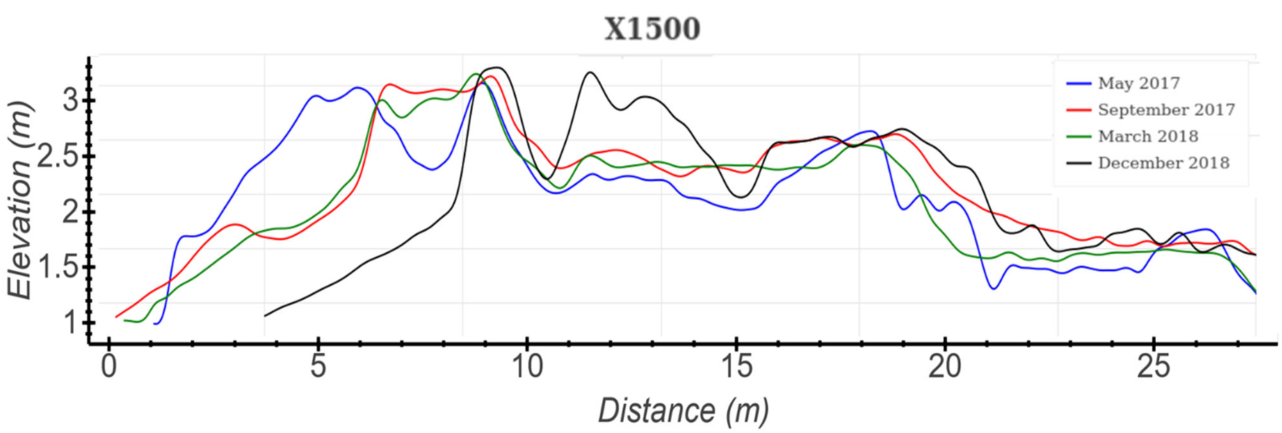

Figure 32: Cross-shore Profile X1500. Dune retreat also occurred between May 2017 and September 2017. The dune crest remained in March 2018, and the dune crest experienced significantly less retreat than X1300.

extent of dune withdrawal between March and December 2018. This dune withdrawal further suggests that although Harvey did not cause extreme geomorphological changes, the minor damage it caused to the dunes, along with the increase in sediment from the increased river discharge, led to major changes in the dune morphology at some point after the storm subsided.

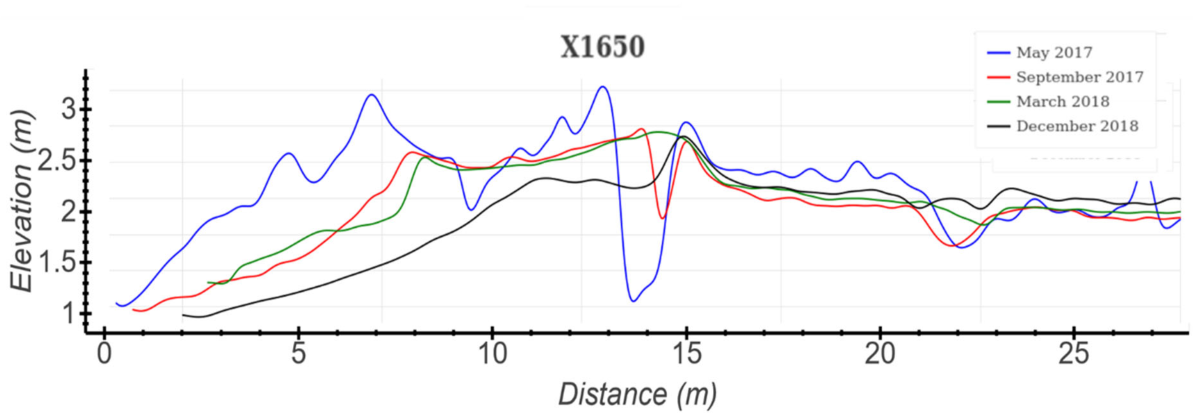

Figure 35: Cross-shore Profile X1650. This profile was taken near Site B. The dune crest reaches a height of 3 m, and the dune has developed a smoother slope between May 2017 and March 2018. The smoothing is due to dune loss from the dune blowout at Site B.

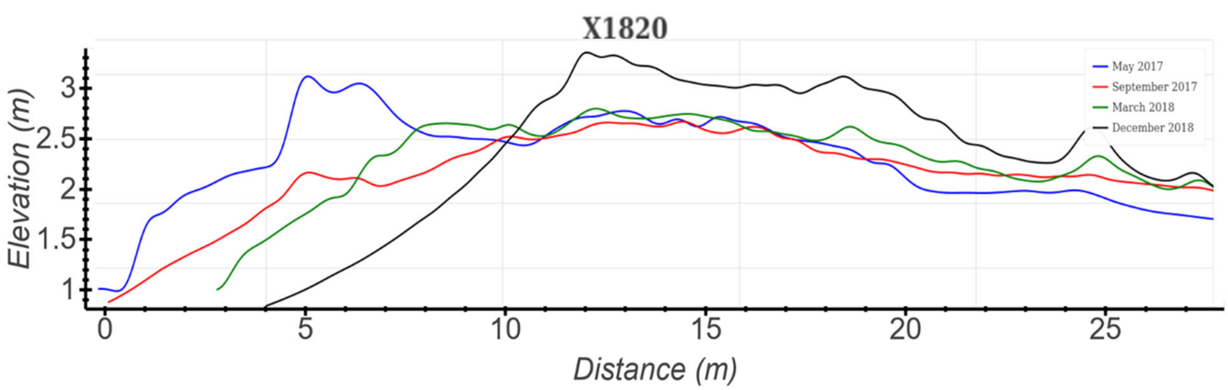

Figure 37: Cross-shore Profile X1820. The dune ridge shrank almost a meter during Hurricane Harvey, which indicates this area was hit harder than the delta region. The area suffers from a noncontinuous dune ridge, which increases the surface area exposed to storm forces. The backdune lagoon also limits available space for the backdune region to develop, also weakening the dunes.

X1650 (Figure **30**) shows a response similar to that of X1500. There was a significant loss of sediment at the shorefront and dunefront brought on by high winds and storm surge.

However, the resulting September profile exhibits a less steep profile than does X1500. As a result, the March 2018 profile maintained a relatively stable dune crest.

The dunes in the delta region are small, ranging between 1 and 1.5 m in height. The small dunes make this region more vulnerable to the effects of even minor storm surge.

Moving further east along the beach, profile X1820 (Figure **30**) shows a dune profile taken near Site B. The dune ridge shrank almost a meter during Hurricane Harvey, which indicates that this area was hit harder than the delta region. Because this area suffers from a noncontinuous dune-ridge, this increases the surface area exposed to storm forces. This region also hosts a lagoon that has appeared and disappeared several times since 2000 (Carlin et al., 2014). The lagoon is mostly tidally dominated. However, sediment has been increasingly deposited in a fan stemming from the breach in the dunes.

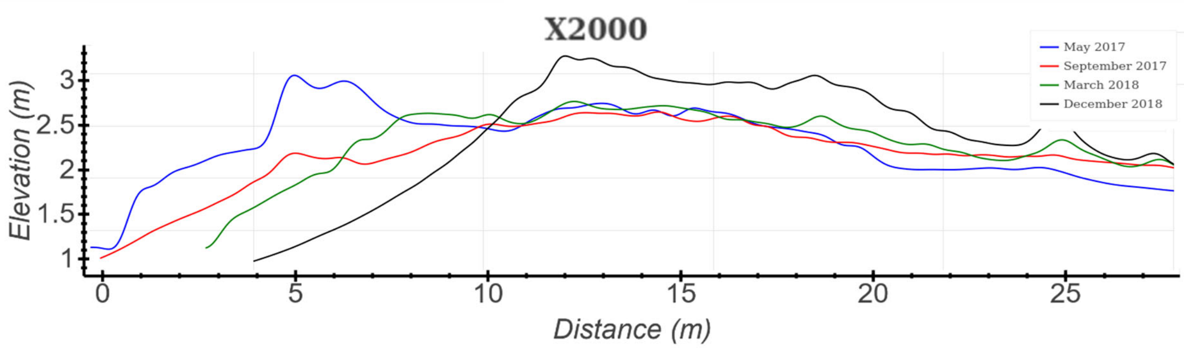

*Figure 38: Cross-shore Profile X2000. The track was measured between the two breaches between the dunes shown in Site B (Figure **25**). The dunes were significantly taller in May 2017, at about 3.5 m. The dunes show a height difference of about 1 m compared to X1820, but lie only 180 m apart.*

The deposition implies that larger storm surges and seasonal waves appear to be depositing sediment in the lagoon. Therefore, wave action may be contributing to the evolution of the lagoon as well. The presence of the lagoon also allows less room for secondary dunes to form behind the primary dune, shoreside of the lagoon.

Track X2000 (Figure **31**) was taken between the two breaches to the dunes shown in Site B (Figure **25**). As is evident, the dunes were significantly taller in May 2017, at about 3.5 m. This larger size shows the discrepancy between this track and X1820, which was measured close to the dune breaches. The dunes show a height difference of about 1 m but lie only 150 m apart. The height difference highlights the significant impact that can be observed in a dune regime that experiences any breaching. The area immediately surrounding the dunes is the most vulnerable.

The dunes in X2000 appear to have been resilient to Hurricane Harvey, because the dune crest in September 2017, following Harvey, stood at about 2 m in elevation. Between September 2017 and March 2017, the dune crest remained stable, and little movement was measured. However, as in the other profiles, between March 2018 and December 2018, there was a degree of dune withdrawal. Here, it appears that the dune shrunk and withdrew slightly. Even with its diminished size, due to the dunes starting at a much healthier and larger state in May, the dunes still reached a height of about 2 m, double that of the previous profiles.

As was evident in X1500 and X1300, the presence of a large secondary dune behind the dunefront helped stabilize the beach profiles. The lagoon impedes the formation of backdunes that could provide further protection when the foredune is damaged during storms. Furthermore, if stronger storms penetrate inland through the breaches, it could cause erosion and coastline loss for the wetlands surrounding the lagoons. Just as a narrow beachfront reduces the likelihood of the formation of incipient dunes, which could further reinforce the shoreline, the lack of area for backbeach expansion causes these dunes

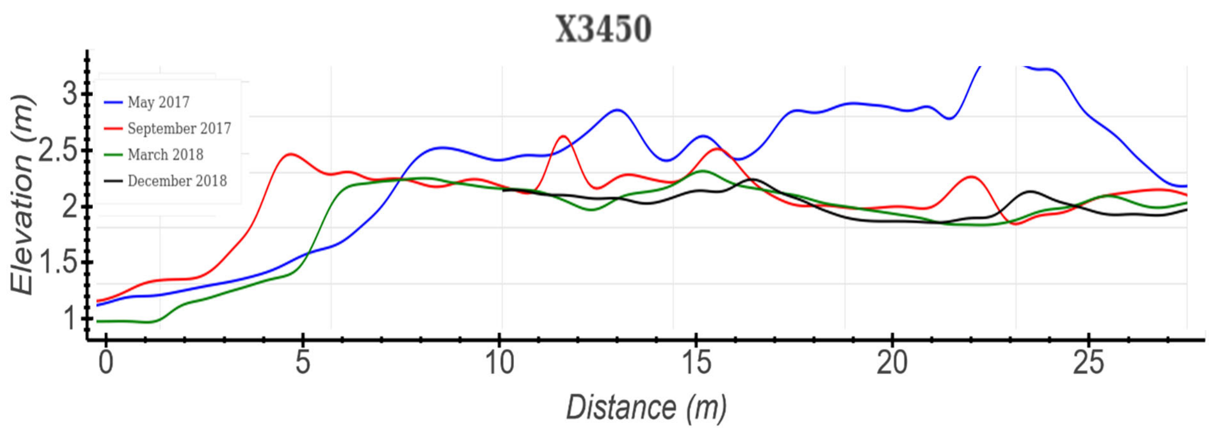

Figure 39: Cross-shore Profile X3450. This region has received more replenishment attention than the delta region, allowing it to withstand dune damage more

to be at risk (Puijenbroek, 2017). We now examine beach profiles further east along the shoreline to determine if the entire beach was similarly affected by Harvey.

Figure **32** shows X3450, which was taken near Site A. This area differs from the delta region in some key respects. This region has received more replenishment attention than the delta region, as is evident from pine trees that were planted along the dune ridge in some locations. These trees have allowed the dunes to remain much more stable, because the thicker tree roots help keep the dune sediment in place. As Figure **32** shows, the dunes in this profile are much taller than the dunes in the delta region. The dune crest in May 2017 stood at more than 3.5 m and stayed at that elevation even during Hurricane Harvey. The dune crest remained stable through the winter into March 2018; the crest, however, returned to its pre-storm position by December 2018.

The presence of human-made reinforcements in form of the pine trees allowed this dune profile to recover its dune crest nearly back to its pre-storm location. The large discrepancy between X3450 and the other profiles near the delta region shows the impact even small amounts of artificial reinforcement can have on a dune regime. Moreover, by December 2017, the shore extended beyond its pre-storm location, indicating successful recovery (Morton

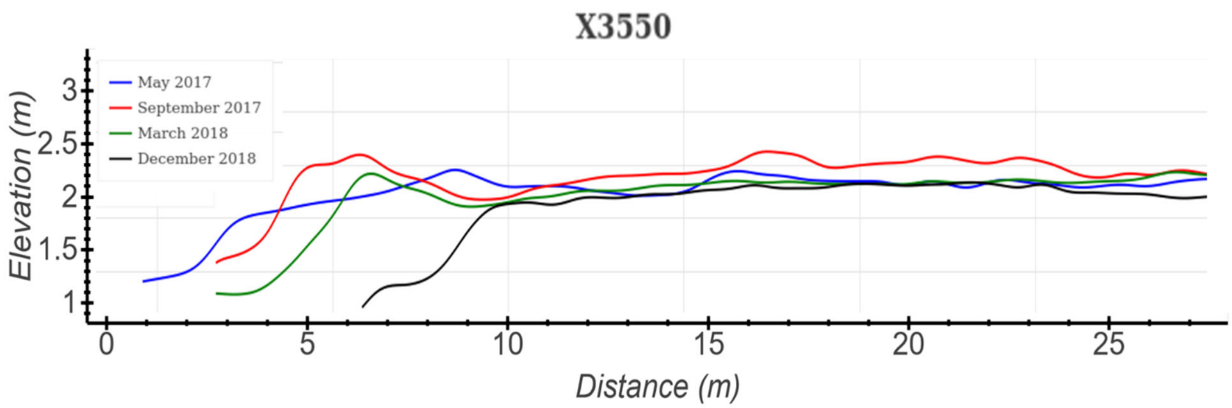

Figure 42: Cross-shore Profile X3550. This region has received more replenishment attention than the delta region, allowing it to withstand dune damage more effectively.

and Mckenna, 1999). These dunes also have a healthy backdune region, which is taller than the foredune and can help provide further stability for the entire profile. The dunes in X3550 (Figure **33**) are similar to the dunes in X3450, with a gradual slope leading up to a dune crest approximately 2 m high. The dune crest experienced little movement between May 2017 and March 2018. However, the dune profile advanced about 20 m between March 2018 and December 2018. Moreover, the dunes show a healthy profile, with a distinguishable beachfront, foredune, and backdune area. Hurricane Harvey appeared to have little impact on the dunes in this profile, although it is likely that some bulldozing was undertaken to clear debris onshore from the storm. Clearing debris also assists in dune resilience by helping to create the gently sloping profile artificially. Additionally, debris such as logs is bulldozed and deposited on the dune crest, which can further help reinforce it.

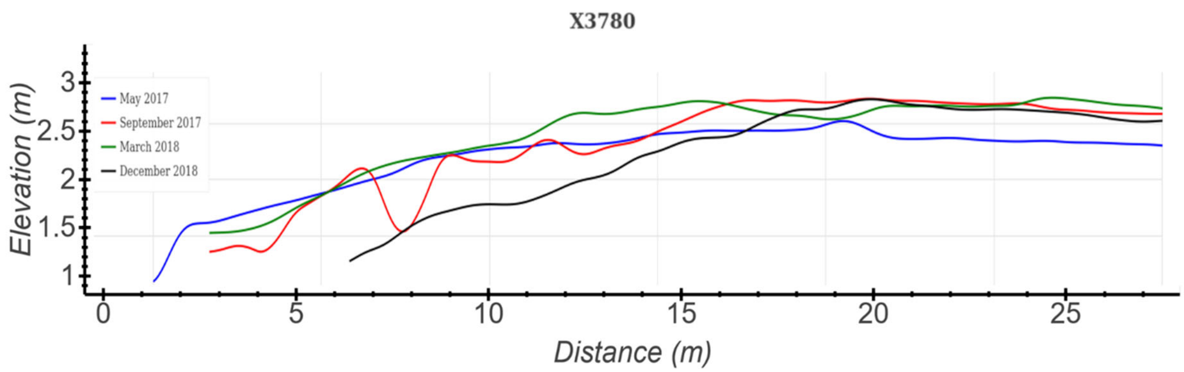

Figure 43: Cross-shore Profile X3780. This region has also received more replenishment attention than the delta region, allowing it to withstand dune damage more effectively.

This is in stark contrast to X3780 (Figure **34**), which experienced significant dune advance and buildup between March 2018 and December 2018. Once passing Site A, the beachfront width increases significantly, which is a major determining factor of the survival of a dune (Claudino-Sales et al., 2008). Less wave energy hitting against the dune results in greater survivability of the dune and increased chances of recovery after a storm event. As is evident in the tracks, both from the delta region and moving east along the beach, the dunes past Site A moving west have remained much healthier and stable than the dunes and beach southwest of Site A. Site A is notable in that the beachfront width changes quickly at this point. The width change is partly due to a lack of dune movement resulting from the planted vegetation and a lack of replenishing sediment on the beachfront. The dunes located further east from Site A show more dune withdrawal, but they also have a more well-developed beachfront and were therefore able to return to their pre-storm state much more rapidly.

Lastly, X4000 (Figure **35**) shows the strongest dunes out of all the compared profiles. The pre-storm dune crest stood at about 3 m, with a well-graded slope leading up to the crest from the shoreline. Harvey did cause some steepening of the dunes, probably from scarping, but they quickly regained their pre-storm location and elevation by March 2018. However, the

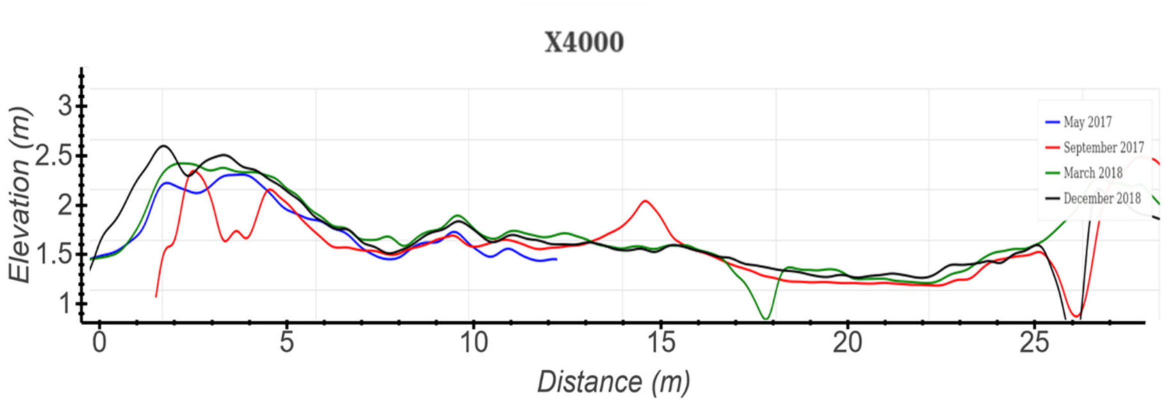

Figure 44: Cross-shore Profile X4000. This region has received more replenishment attention than the delta region, allowing it to withstand dune damage more effectively.

dune was significantly flattened by December 2018. The flattening may have been caused by increased wave action, as in the other profiles, but the profile also appears more resilient to the effects of storms and erosion and may simply be following more natural patterns of dune retreat and advance. Hall and Halsey's (1991) study of dune response to Hurricane Hugo in

1989 indicated that only high and continuous dune sections provided a solid barrier against storm surge and overwash.

This study's analysis of the results of the different tracks taken along Bryan Beach makes evident a stark difference between the dunes to the left and the dunes to the right of Site A. The dunes to the right of Site A show typical signs of storm damage and replenishment. They maintained a relatively stable dune crest height and showed signs of partial, if not full, recovery by December 2018. This is likely the result of several factors:

1. The areas between Site A and the beach entrance located at X4000 were replenished between 2014 and 2016. The replenishment included the planting of pine trees and other vegetation to fortify the dunes and prevent them from migrating.
2. This area was also bulldozed following Hurricane Harvey (Figure **38**). The effects of bulldozing, as discussed above, help maintain a good beach profile with an increased slope, which in turn helps to mitigate some of the effects of stronger incident waves. Because these areas have a wider beachfront width, the swash zone is distant from the dune toe, and thus much of the force from incident waves is dissipated before reaching the dune toe.
3. The Quintana Jetty blocks a significant amount of sand and coarser-grained sediments from reaching areas closer to the delta. As is evident from the exposure of clay at Site A, the sand supply appears to diminish with increasing distance from the Quintana Jetty following the direction of the longshore drift.

Because areas close to the beach entrance have seen more regular maintenance and replenishment by State Park authorities and the Texas GLO, they showed fewer effects caused by Hurricane Harvey, despite the storm's fairly long duration. Harvey never made landfall near Freeport, so the storm surge remained relatively small and did little damage to the artificially fortified beach profiles. This apparent lack of beach damage shows that even small amounts of human fortification can have a positive impact on beach dunes, and more fortifications should be implemented in the future. The bulldozing also had a positive effect on this beach area by clearing debris and increasing the width of the beachfront. Cleared debris is often deposited on top of the dune crest, which provides it with further stability. However, as X3450 and X3570 showed, keeping sections of the dune in place can be detrimental as well.

Just as with relative coastline retreat that is caused by the ground sinking relative to the shoreline, Site B's shorefront has significantly shrunk, while the dunes have not moved to accommodate the new shoreline and maintain a larger beachfront width. X3570 experienced much more dune crest retreat, but that retreat kept the shorefront width larger and appeared to have played a role in allowing the dunes to recover as they did. It is even possible that the placement of pine trees disrupts the advance and retreat of dunes, which do not allow the entire dune regime to adapt to the change in beachfront width.

The change in beachfront width is due to the Quintana Jetty, which blocks sand and courser sediment from reaching far past the jetty. Because the longshore current must travel around the jetty, only smaller-grained sediments can remain entrained, even when the current slows down and is blocked by the break-water structure. Sediment size is also a factor that can help determine dune survival (Claudino-Sales et al., 2008). Claudino-Sales et al. investigated several dunes on Florida beaches and found that dunes consisting of coarser grain sizes were more likely to survive than dunes consisting of smaller grain sediments. Moreover, CHIRP imaging of the delta undertaken in another study shows that the right flank of the delta consists of 45% coarse-grained sediment (> 45 mu), whereas the left flank consists of approximately 60% coarse sediment. Furthermore, the mean grain size for the right flank is around 30 μm, and the left flank has an average grain size of 40–90 μm, depending on the measured area (Carlin et al., 2014).

4.6: Volume Change Calculations

This study uses metrics introduced by Morton (1994), in which beach recovery was defined as replenishment of the total percentage of sediment lost during a storm. Volume calculations performed on the DEMs in GMT show that there was a 25% loss in sediment between May 2017 and September 2017 along the entire 7-km study area. By March 2018, the study area had fully recovered the percentage of sediment lost and gained an additional 101,450,886 cubic meters of sediment (Figure **36**). The 25% loss in volume between May and September 2017 was mostly due to Hurricane Harvey. However, between September 2017 and March 2018, the 7-km beach area regained the percentage of sediment lost and also gained an additional 101,450,886 cubic meters by March 2018. Figure **36** presents volume calculations taken from May 2017 to September 2017 (top) and September 2017 to March 2018 (bottom). Blue represents areas of sediment gain, and red indicates areas of sediment loss.

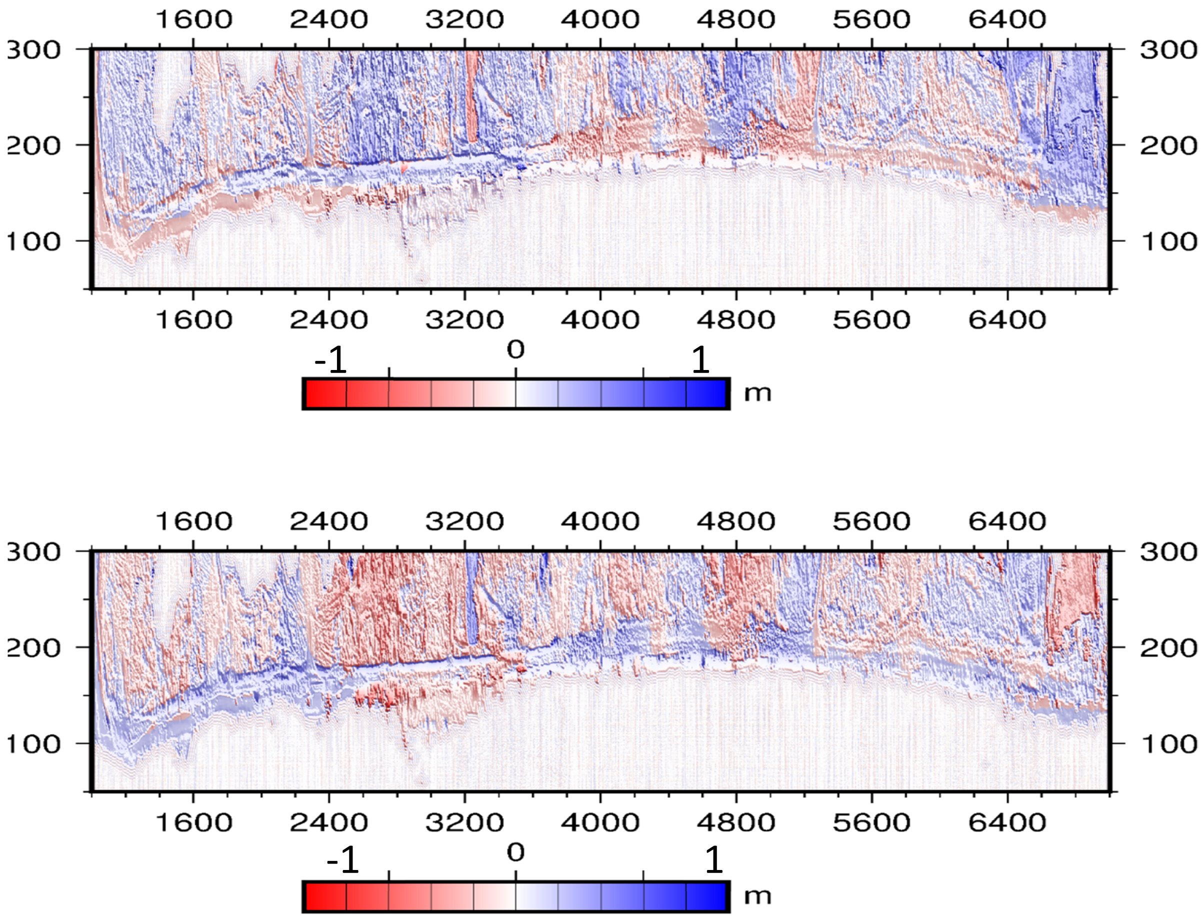

Figure 48: (top) May 2017–September 2017 Beach Volume Difference.

(bottom) September 2017–March 2018 Beach Volume Difference. Red indicates areas of erosion, and blue indicates areas of accretion.

Chapter 5: Discussion

The right and left halves of the beach show a vast difference in beach health. However, the entire 7-km region has been subjected to the same coastal forces. The discrepancy in beach health can be attributed to disruptions in natural sedimentation systems and human intervention. The right half of the beach was replenished between 2014 and 2016. Besides replenishing sediment, the replenishment program included fortification of dunes with wooden emplacements and planting of vegetation (Durnin, 2019). These fortifications have kept the dunes in this area much more stable and capable of withstanding erosive forces. The Bryan Beach Park management has also bulldozed sediment up onto the dunes on several occasions. The left half, however, was not included in the replenishment area, and little maintenance appears to occur in that area. The dunes on this side are simply showing the results of uninterrupted coastline loss. Figure **35** shows photos taken of both halves of the beach on September 9, 2019. The right half of the beach has much healthier vegetation than the left half.

Bulldozing also has undesired effects on the beach profile (Figure **36**), because it destroys any incipient dunes that may be forming. The formation of incipient dunes is another indicator of beach health that is wiped away due to human modifications on Bryan Beach.

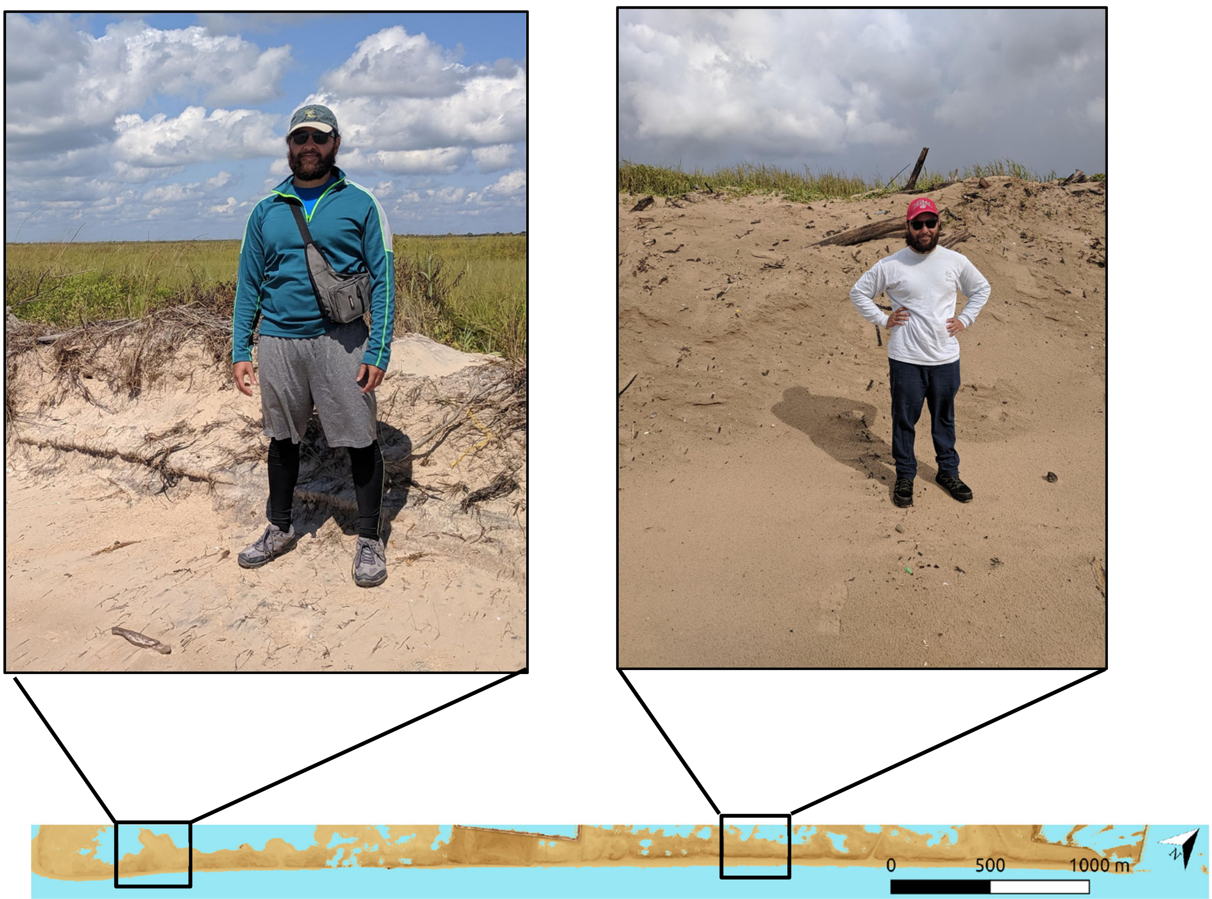

Figure 50: Dune Height Difference between Different Beach Sections. Due to lack of replenishing sand blocked by the jetty and lack of sediment from the Brazos River resulting from the salt wedge and the longshore drift, the dunes near the delta region have almost disappeared. They may recover, because the delta bar has continued accreting since Hurricane Harvey.

The left half of the beach does not receive as much natural sediment as the right half. This is because the Freeport Harbor Jetty blocks sediment along the longshore current from reaching this area (Figure **2**). The right half of the beach is also affected by the jetty, but since it has been replenished the effects from the jetty are not as noticeable.

Figure 51: Bulldozing at Bryan Beach Near Freeport, Texas. The bulldozing widens the beachfront..

The right half also receives less replenishing sediment from the Brazos River. The presence of a salt wedge in the Brazos River Delta blocks sediment from the Brazos River from reaching the

Gulf of Mexico and entering the longshore current (Carlin et al., 2014). Consequently, the lack of larger grain sediments on the right flank of the Brazos River leads to weakening of the beach dunes.

As noted above, CHIRP imagery shows a significant difference in the mean grain size between the right and left flanks of the Brazos River Delta. A study of barrier islands off the Coast of Florida showed that dunes with smaller grain sizes were more vulnerable to erosive forces and therefore smaller in size compared to sand dunes composed of larger grain sizes (Claudino-Sales et al., 2008). As with the Florida example, the smaller size of dunes near the delta region may be due to a lack of course grain

Figure 53: Contrast between Site A Dunes and Dunes Close to the Beach Entrance Near the Quintana Jet

sediment (Claudino-Sales et al., 2008). Furthermore, field observations and CHIRP measurements from Carlin et al. (2014) show that grain size appears to decrease with increasing distance from the Quintana Jetty.

Salt-wedge estuaries are the most stratified of all estuary types and often occur in shallow deltas with large tidal and freshwater velocities (Ralston et al., 2010). Salt-wedge estuaries are typically dominated by high flowing river discharge and weak tidal and wave forces (Carlin et al., 2014). A salt wedge can be defined by salinity differences of greater than 20

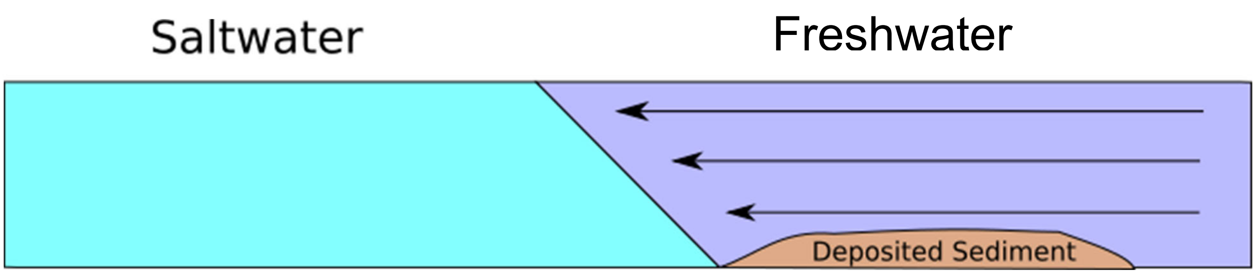

Figure 55: Diagram Demonstrating Formation of an Estuarine Salt Wedge. The wedge forms due to high water density stratification.

pus across a few meters in the vertical direction and less than 500 m in the horizontal direction (MacDonald and Geyer, 2004). When the high flowing freshwater meets the saltwater, the difference in buoyancy causes a highly stratified wedge to form (Figure **37**). As sediment is transported down the river, it can become caught between the outgoing and incoming flow (Carlin et al., 2014). The high stratification consequently causes a buildup of sediment on the river bottom upshore of the wedge.

As stated in Carlin et al. (2014), several cruises have been undertaken to measure CHIRP and water column in several locations throughout the Brazos River. Conducted in 2007, 2010, and 2012, these sampling cruises started 12 km upriver from the Brazos River Delta and ended 6 km out to sea from the delta. Water-column measurements were taken with a Sea-bird Electronics SeaCAT Profiler CTD SBE 19plus and an RBR XR-420 CTD with OBS (Carlin et al., 2014). Salinity measurements from the water-column measurements indicated the presence of a salt wedge in the delta (Carlin et al., 2014). During one cruise, the river discharge was measured at ~243 m^3/s, and an isohaline that reached 3 km upriver was identified (Carlin et al., 2014). Another cruise indicated that the isohaline reached 6.5 km upriver during a discharge of 290 m^3/s. After peak flooding on July 12, 2007, discharge was recorded at 1600 m^3/s, and the isohaline was not detected. Furthermore, CHIRP measurements taken during the cruises indicated the presence of a mud layer when the salt wedge was present in the Brazos River (Carlin et al., 2014).

Sediment discharge to the Gulf of Mexico is therefore highly dependent on the presence of the salt wedge (Figure **40**) (Carlin et al., 2014). Past observations confirm that the salt wedge achieves its farthest reach out to sea when river discharge is at its highest. When river discharge is low, the salt wedge intrudes inland, and sediment is trapped upstream. Low wave forces at the delta allow the longshore current to dominate flow in the river mouth and carry sediment towards the left flank of the delta (Figure **41**) (Carlin et al., 2014).

The salt wedge in the Brazos River was shown to intrude out to sea when river discharge exceeded 400 m^3/s (Carlin et al., 2014). Figure **4** plots gauge height and discharge between January 1, 2017, and April 1, 2018, at the gauge station in Rosharon, Texas. Between January 2017 and April 2018, discharge exceeded 400 m^3/s only during Hurricane Harvey. The storm water produced enough force to displace large chunks of sediment. The storm probably also washed out sediment that was entrapped by the wedge and had been deposited as a mud layer upstream (Carlin et al., 2014; Nengwang, 2018). This is further made evident by the appearance of a red tide in the river mouth on September 9, 2017, following the cyclone. The tide was likely caused by the rapid influx of nutrients that were swept up by Hurricane Harvey (Nengwang,

Figure 56: Diagram Illustrating Salt-wedge Formation in the Brazos River Delta. Low river discharge causes a salt wedge to form at the Brazos Delta. The slowdown of sediment at the density boundary of the wedge allows the longshore drift to dominate and deposit sediment on the left flank of the delta (imagery from Google Earth Pro).

2018). In addition, between May 2017 and September 2017, the delta region gained sediment that was likely flushed out from the river by the increased river discharge (Figure **4**).

The presence of this salt wedge could have far-reaching implications for the deltaic system. The amount of landward intrusion of the salt wedge (Figure **41**) has a direct effect on the amount of sediment that reaches the coast. When river discharge is high, the salt wedge is pushed further out to sea, and more sediment reaches the coast. Conversely, when river discharge is low, the salt wedge intrudes upriver.

The various cross-sections show that dune morphology exhibits clear differences depending on the distance from the Quintana Jetty, and Figure **39** compares the results of artificially planted vegetation and natural vegetation. The additional reinforcement provided by the extra vegetation and wooden supports has reinforced the dunes. However, artificially planted pine trees appear to be detrimental to beach health. Although the pine trees reinforce the dune, they do not allow dune landward retreat to compensate for coastal loss, resulting in narrowing of the beachfront (Figure **13**).

Beach recovery can be divided into four stages (Morton, 1994; Owen 2017), as follows:

1 Initial storm erosion causes substantial erosion and moves the profile landward. Subsequently, forebeach accretion and flattening begin during the initial recovery after a storm event.

2 Backbeach aggradation begins when widening of the beach profile allows sand to start accumulating in the backbeach, and backshore steepening becomes visible.

3 Steepening and stability of the backbeach allow for initial dune rebuilding.

Initial forebeach accretion following storm events is generally a result of offshore bars fusing to the beach face (Owen, 2017). Expansion of the beach face triggers initial beach recovery by allowing the dunes to stabilize and providing new ground for the development of incipient (embryo) dunes ahead of the established foredunes (Puijinbrock et al., 2017). However, due to the conditions at the delta caused by the salt wedge and by the longshore drift, offshore bars that form at the mouth of the river are swept up in the current and deposited on the left flank of the delta. Beach recovery can also vary along with the horizontal beach profile, depending on differences in dune height and gaps (Owen et al., 2017). In areas with smaller dunes that experience wave overwash, dunes can be eroded entirely, whereas more massive dunes can suffer erosional scarping at the dune base. Erosional scarping creates a much steeper dune profile, leading to an unstable dune topography and dune blowouts. Wind speed typically increases across blowouts, further amplifying aeolian erosion (Otvos et al., 2017).

Due to the changes in buoyancy at the river mouth, a salt wedge forms, which causes river sediment to be deposited further upstream. The amount of intrusion inland by the salt wedge is primarily determined by river discharge (Carlin et al., 2014). The Brazos River has fairly low river discharge due to human damming and water usage. During Hurricane Harvey, however, the massive increase in water discharge occasioned by increased rainfall appears to have flushed out the salt wedge and brought new sediment to the river mouth.

River discharge during Hurricane Harvey was elevated for a period above levels required to wash out the salt wedge (Carlin et al., 2014). Until March 2019, river discharge never reached

400 m^3/s following Hurricane Harvey. As a result of the low discharge during the replenishment period, the western region of the beach was sediment starved due to the reemergence of the

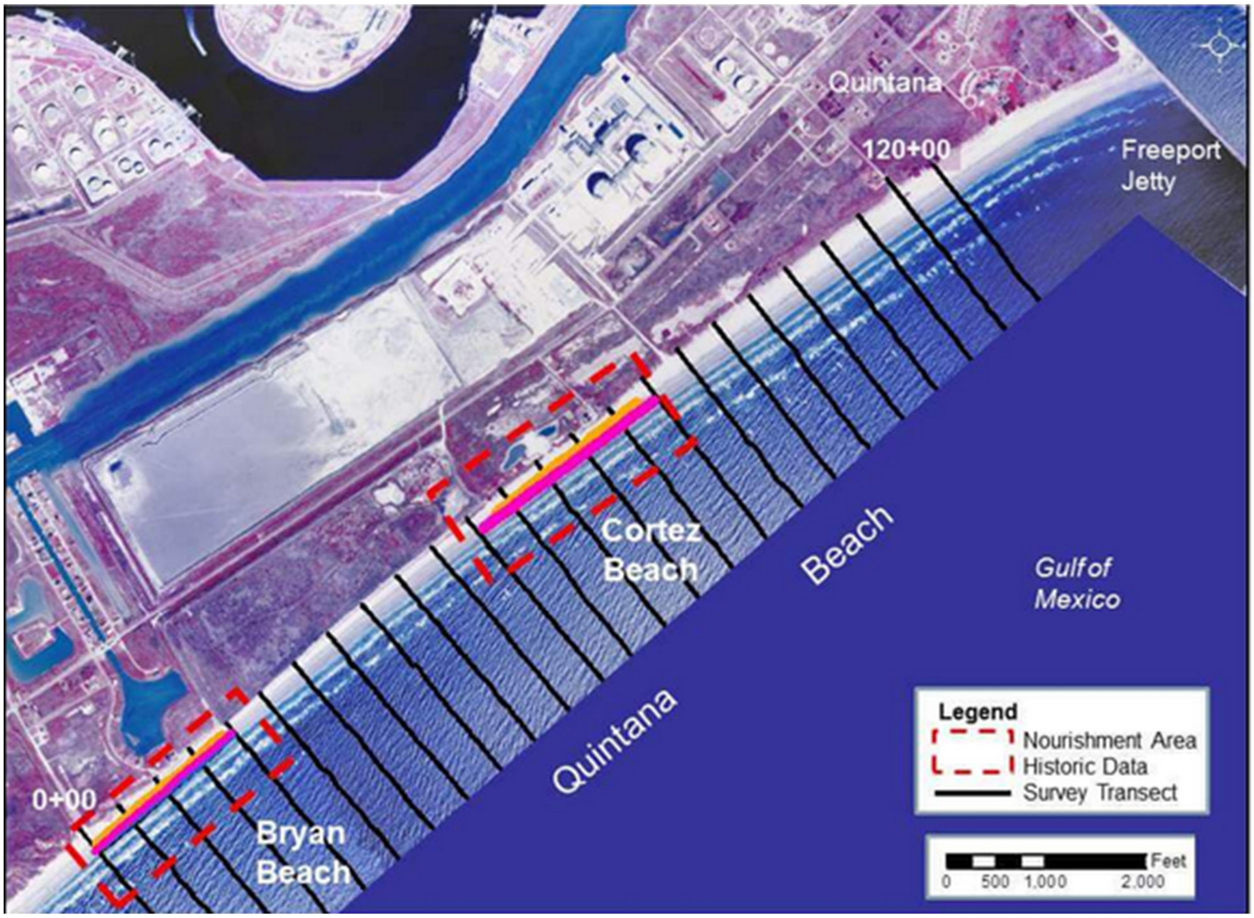

Figure 58: Targeted Replenishment Areas on Bryan Beach, 2014–2016. Bryan Beach was replenished previously, between 2014 and 2016. The figure shows the areas that were replenished. Imagery from CHRGIS (CHRGIS, 2019).

salt wedge.

The Texas GLO continues to monitor Bryan Beach, and it has been noted that the width of the beach has fallen under the GLO's action width. The action width is a specific measurement determined by the GLO that warrants a replenishment program for a section of coastline. Replenishment is scheduled to start in early 2020, but it has yet to be decided which areas will be emphasized. Replenishment is projected to be completed by August 31, 2022, and will repair 563.88 m of coastline (Durnin, 2019). A budget of $697,783 was allocated for the project, down from the $1,605,796.12 budgeted for the replenishment program completed in March 2016.

Chapter 6: Conclusions and Future Work

This study concludes that the morphology of certain regions of Bryan Beach, including the delta, did not show signs of recovery from Hurricane Harvey during the study period. Although the full 7-km study area has regained the sediment volume lost during Hurricane Harvey, the dune-morphology recovery along the beach has been varied, depending on several factors: proximity to artificial coastal fortifications, such as jetties; artificial and natural vegetation; proximity to the Brazos River Delta; artificial sediment replenishment; and amount of sediment replenished through littoral transport. Hurricane Harvey affected the beach morphology of the eastern flank of the Brazos River as well as the dunes in Site A and Site B. The hurricane brought record floods, which drastically increased the Brazos River's discharge rate. However, the volume of water that passed through the delta appears to have been enough to cause the emergence of a mouth bar. This mouth bar could continue to grow given the right conditions and river discharge, or it could be deposited on the west flank of the delta by the longshore current, resulting in another ridge. Hurricane Harvey also exacerbated dune damage that was sustained years earlier, during Hurricane Ike in 2008. Hurricane Ike hit Bryan Beach much more directly, and the dunes therefore sustained more substantial damage.

However, the dunes never fully recovered from this damage, and the dune breaches became gaps in the dune front, aided by erosive forces and continuing tropical storms. These breaks in the dune front weakened the dunes' resilience to further beach erosion.

Furthermore, observations show that during high tide, a significant portion of the sand layer is removed and exposes the underlying clay (Figure **23**). This is a hazard to beachgoers, who often become stuck in the clay and mud. Like the effects from seawalls, waves hit the steep dune topography and can reflect out to sea, additionally limiting the sediment available down the longshore current. Figure **23** also shows that the beachfront significantly narrows as it travels southeast to the delta from Site A. However, this study observed only immediate effects, that is, those within about one year after Hurricane Harvey. Long-term storm recovery can take 10+ years, so further monitoring of Bryan Beach is necessary (Morton and Mckenna, 1999; Eismann et al., 2018).

Bryan Beach should continue to be monitored throughout the replenishment process scheduled by the Texas GLO. We should identify which areas need to be replenished and continue producing dune profiles in both replenished and nonreplenished areas to better evaluate the impact of the GLO's repair efforts. Moreover, more effort should be devoted to accurately scanning the pine trees shown in Figure **14,** as well as the Brazos Delta, to monitor the advance and retreat of the current mouth bar. Small boreholes can be dug on the beach to reveal the sand and underlying clay layer. Several holes can be dug near the Quintana Jetty, progressively moving towards Site A. The sand-layer thickness can be measured to determine if the sand layer becomes thinner with increasing distance from the jetty. This would provide further evidence that the jetties are in fact blocking sand from reaching areas southeast of Freeport Harbor.

Bibliography

ASPRS. Available online: https://www.asprs.org/a/society/committees/standards/asprs_las_format_v12.pdf (accessed on 05, December, 2019).

Blake, E. S.; Zelinsky, D. A. National Hurricane Center Tropical Cyclone Report: Hurricane Harvey (AL092017). **2017**.

Carlin, J. A.; Dellapenna, T. M. (2015). The evolution of a subaqueous delta in the Anthropocene: A stratigraphic investigation of the Brazos River Delta, TX USA. *Continental Shelf Research* **2015**, *111*, 139–149.

CEPRA Beach Monitoring Program and Coastal Habitat Restoration GIS (CHRGIS). Available online: https://cbi.tamucc.edu/CHRGIS/ (accessed on 10 December 2018).

CloudCompare (version 2.9.1) [GPL software]. Available online: http://www.cloudcompare.org (accessed on 10 August 2017).

Durnin, T. (Texas General Land Office, Austin, TX, United States). Personal communication, **2019.**

Eisemann, E. R.; Wallace, D. J.; Buijsman, M. C.; Pierce, T. Response of a vulnerable barrier island to multi-year storm impacts: LiDAR-data-inferred morphodynamic changes on Ship Island, Mississippi, USA. *Geomorphology* **2018,** *313*, 58-71.

Fernandez-Diaz, J. C., Carter, W. E.; Glennie, C.; Ramesh S. L.; Pan, Z.; Ekhtari, N.; Singhania, A.; Hauser, D.; Sartori, M. Capability Assessment and Performance Metrix of the Titan Multispectral Mapping LIDAR. *Remote Sensing* **2016**, *8*.

Ferraz, A., B, F; Jacquemoud, S.; Gonçalves, G. The Role of Lidar Systems in Fuel Mapping, **2019**.

Galbraith, R. J. R.; Clough, J. S.; Harrington, H.B.; Page, G. Global climate change and sea level rise: Potential losses of intertidal habitat for shorebirds, **2002,** *Waterbirds*, *25*, 173-183.

Germiat, S J.; Sharp, J. M. Assessment of future coast land loss along the Upper Texas Gulf Coast to the year 2050. *Environmental and Engineering Geoscience* **1990,** *27*, 263–280.

Glennie, C. L.; Carter, W. E.; Shrestha, R. L.; Dietrich, W. E. Geodetic Imaging with Airborne LiDAR. *The Earth's Surface Revealed* ***2013****, Reports on Progress in Physics*, 76.

Guzman, V. Deriving Morphological Changes in the Eastern Flank of the Brazos River Delta Using Terrestrial Laser Scanning and GPS. Master’s Thesis, University of Houston, **2017**.

Hall, M.; Halsey, S. Comparison of overwash penetration from Hurricane Hugo and pre-storm erosion rates for Myrtle Beach and North Myrtle Beach, South Carolina, U.S.A. *Journal of Coastal Research* **1991**, 229–235.

Hardin, E.; Kurum, O.; Mitasova, M.; Overton, H; Margery, F. Least cost path extraction of topographic features for storm impact scale mapping. *Journal of Coastal Research* **2012**, *28,* 970-978.

Hesp, P. Foredunes and blowouts: Initiation, geomorphology and dynamics. *Geomorphology* **2002**, *48*, 245-268.

Houser, C.; Wernette, P.; Rebtschlar, E.; Jones, H.; Hammond, B.; Trimble, S. Post-storm beach and dune recovery: Implications for barrier island resilience. *Geomorphology* **2015**, *234*, 54-63.

Hulme, M.; Mahony, M. Climate change: What do we know about the IPCC. *Progress in Physical Geography* **2010**, *34*, 705-718.Hurst, M. D.; Barkwith, A.; Ellis, M. A.; Thomas, C. W.; Murphey, B. A. Exploring the sensitivities of crenulate bay shorelines to wave climates using a new vector-based one-line model. *Journal of Geophysical Research: Earth Surface* **2015**, *120*, 2586-2608.

Jeffrey, P. G. Subsidence of the Texas coast: Inferences from historical and late Pleistocene sea levels. *Tectonophysics* **1993**, *222*, 445-458.

Kearns, T. J.; Wang, G.; Bao, Y.; Jiang, J.; Lee, D. Current land subsidence and groundwater level changes in the Houston Metropolitan Area (2005–2012). *Journal of Surveying Engineering* **2015**, 141.

Kearns, T.; Wang, G.; Turco, M.; Welch, J.; Tsibanos, V.; Liu, H. Houston16: A stable geodetic reference frame for subsidence and faulting study in the Houston Metropolitan Area, Texas, U.S. *Geodesy and Geodynamics* **2018**, *10 .*

Kempeneers, P.; Deronde, B.; Provoost, S.; Houthuys, R. (2009) Synergy of airborne digital camera and Lidar data to map coastal dune vegetation. *Journal of Coastal Research* **2009**, *53*, 73-82.

MacDonald, D.G.; Geyer, W.R. Hydraulic control of a highly stratified estuarine front. *Journal of Physical Oceanography* **2005**, *35*, 374-387.

Morton, R. A. Stages and durations of post-storm beach recovery, Southeastern Texas Coast, U.S.A. *Journal of Coastal Research* **1994**, *10*, 884-908.

Morton, R. A.; McKenna, K.K.; Crowell, M.; Leatherman, S. P. Analysis and projection of erosion hazard areas in Brazoria and Galveston Counties, Texas. *Journal of Coastal Research* **1999**, *28*, 106-120.

Mosa, A.; Schon, B.; Bertolotto, M.; Laefer, D. Evaluating the benefits of octree-based indexing for Lidar data. *Photogrammetric Engineering and Remote Sensing* **2012**, *78*, 927-934.

Nengwang, C.; Krom, D.; Wu, Y.; Yu, D.; Hong, H. (2018). Storm induced estuarine turbidity maxima and controls on nutrient fluxes across river-estuary-coast continuum. *Science of the Total Environment* **2018**, *628*, 1108-1120.
Otvos, E. G. Rain-induced beach processes: Landforms of ground water sapping and surface runoff. *Journal of Coastal Research* **1999**, *15*, 1040-1054.

Owen, B.; Lentz, T.; Erika, E.; Hapke, C. J.; Henderson, R. E.; Wilson, K. E.; Nelson, T. R. Characterizing storm response and recovery using the beach change envelope: Fire Island, New York. *Geomorphology* **2017,** *300*, 189-202.
202.

Paine, J. G. Subsidence of the Texas Coast: Inferences from historical and late Pleistocene sea levels. *Tectonophysics* **1993**, *222*, 445-58.

Puijenbroek, M. E. B.; Limpens, J.; Groot, A. V.; Michel, J. P. M.; Gleichman, R. M.; Slim, P. A.; Dobben, H. F.; Berendse, F. Embryo dune development drivers: Beach morphology, growing season precipitation, and storms. *Earth Surface Processes and Landforms* **2017**, *42*, 1733-744.

Ralston, D. K.; Geyer, W. R.; Lerczak, J. A. Structure, variability, and salt flux in a strongly forced salt wedge estuary. *Journal of Geophysical Research, Oceans* **2010**, 1978-2012, 115.

Rodriguez, A. B. B.; Hamilton , M. D. D.; Anderson, B. Facies and evolution of the modern Brazos Delta, Texas: Wave versus flood influence*.* *Journal of Sedimentary Research* **2000**, *70*, 283-95.

Sweeney, M. R.; Fischer, B.; Wermers, K.; Cowman, T. Eolian and fluvial modification of Missouri River sandbars deposited by the 2011 flood, USA. *Geomorphology* **2018**, *327*, 111-125.

US Army Corps of Engineers. Freeport and Vicinity, Texas Hurricane-Flood Protection Draft Feasability Report. Government report, **2005**.

Wessel, P.; Smith, W. H. F.; Scharroo, R.; Luis, J. F.; Wobbe, F. Generic Mapping Tools: Improved version released, EOS Trans. *AGU* **2013**, *94*, 409-410.

Xiong, L.; Wang, G.; Bao, Y.; Zhou, X; Sun, X; Zhao, R. Detectability of repeated airborne laser scanning for mountain landslide monitoring. *Sensors* **2018**, *19*.

Xiong, L.; Wang, G.; Bao, Y.; Zhou, X.; Wang, K.; Liu, H.; Sun, X.; Zhao, R. A rapid terrestrial laser scanning method for coastal erosion studies: A case study at Freeport, Texas, USA. *Geosciences (Switzerland)* **2019**, *8*.

Wang, G.; Soler, T. OPUS for horizontal subcentimeter-accuracy landslide monitoring: Case study in the Puerto Rico and Virgin Islands region. *Journal of Surveying Engineering* **2012**, *138*, 143-153.

Yilmaz, I. M.; Gullu, M.; Turgut, B. Evaluation of recent global geopotential models based on GPS/levelling data over Afyonkarahisar (Turkey). *Scientific Research and Essays* **2010**, *5*, 484-493.

Zhenpeng, G.; Dai, Z.; Wenhong, P.; Wei, W.; Xuefei, M.; Gu, J.; Li, S.; Huang, H. LIDAR-based detection of the post-typhoon recovery of a meso-macro-tidal beach in the Beibu Gulf, China. *Marine Geology* **2017,** *391*, 127-43.

Zhou, X.; Wang, G.; Bao, Y.; Xiong, L.; Guzman, V.; Kearns, T. Delineating beach and dune morphology from massive terrestrial laser-scanning data using Generic Mapping Tools. *Journal of Surveying Engineering* **2017,** *143*.